MASTER THESIS

Peter Kottman

Modelling of advection-diffusion processes in liver tissue

Mathematical Institute of Charles University

Prague 2023

I declare that I carried out this master thesis independently, and only with the cited sources, literature and other professional sources. It has not been used to obtain another or the same degree.

I understand that my work relates to the rights and obligations under the Act No. 121/2000 Sb., the Copyright Act, as amended, in particular the fact that the Charles University has the right to conclude a license agreement on the use of this work as a school work pursuant to Section 60 subsection 1 of the Copyright Act.

In . . . . date . . . .
                                                        Author's signature

Acknowledgements

Title: Modelling of advection-diffusion processes in liver tissue

Author: Peter Kottman

Department: Mathematical Institute of Charles University

Supervisor: prof. Dr. Ing. Eduard Rohan, Dsc., Mathematical Institute of Charles University

Co-supervisors: Dirk Drasdo, Irene Vignon-Clementel, Inria Saclay Ile-de-France

Abstract: In the modern day, various liver diseases have become increasingly widespread in the human population, some having important mortality rates. Understanding and efficient treatment of these diseases requires a multidisciplinary approach of systems medicine, combining both experimental and modelling fields, as well as clinical practice. As part of such efforts, there have been several studies in the recent years modelling flow and transport in parts of liver micro-architecture. The work presented in this master thesis aims to formulate a descriptive reduced mathematical model of fluorescent marker transport in both sinusoidal and bile canalicular networks in the liver lobule, along with exchanges with neighboring hepatocytes. Motivated by approaches presented in recently published research, we start from a full 3D model for a Class I mixture, present its reduction into 1D equations along the vessel axis, and show proof-of-concept numerical results, discussing further extensions of the model in view of the multidisciplinary research context outlined above.

Keywords: advection-diffusion processes, conservation laws, reduced models, microcirculation, numerical simulations, finite volume method

Názov práce: Modelovanie advekčno-difúznych procesov v pečeňovom tkanive

Autor: Peter Kottman

Ústav: Matematický ústav UK

Vedúci diplomovej práce: prof. Dr. Ing. Eduard Rohan, DSc., Matematický ústav UK

Spoluvedúci: Dirk Drasdo, Irene Vignon-Clementel, Inria Saclay Ile-de-France

Abstrakt: V súčasnosti sa v ľudskej populácii čoraz častejšie vyskytujú ochorenia pečene, pričom niektoré z nich majú vysokú úmrtnosť. Pochopenie a účinná liečba týchto ochorení si vyžaduje multidisciplinárny prístup systémovej medicíny, ktorý spája experimentálne výsledky, teoretické modely a klinickú prax. Súčasťou tohto úsilia je niekoľko nedávnych štúdií modelujúcich prúdenie a transport v častiach pečeňovej mikroštruktúry. Cieľom tejto diplomovej práce je odvodiť deskriptívny redukovaný matematický model transportu fluorescenčných látok v sinusoidách a žlčových kanálikoch v pečeňovom laloku spolu s výmenami s okolitými hepatocytmi. Motivovaní nedávno publikovanými modelmi vychádzame z úplných 3D bilančných rovníc pre zmes triedy I, prezentujeme ich redukciu na 1D rovnice pozdĺž osi modelovej oblasti a uvádzame prototypy numerických výsledkov, pričom diskutujeme o ďalšom rozšírení modelu s ohľadom na vyššie uvedený multidisciplinárny výskumný kontext.

Kľúčové slová: advekčno-difúzne procesy, bilančné vzťahy, redukované modely, mikrocirkulácia, numerické simulácie, metóda konečných objemov

List of Symbols and Abbreviations

Mixture theory

N_A Avogadro's number

$\boldsymbol{b}$ body force

$\mathbb{T}$ Cauchy stress tensor

c_α concentration of the α-th mixture component

$\mathcal{V}$ control volume

ρ density

ρ_α partial density of the α-th mixture component

$\mathcal{M}$ mass of a control volume

m_α mass production of the α-th mixture component

M_α molar mass of the α-th mixture component

n_α number of moles for the α-th mixture component

$\boldsymbol{v}$ velocity

Compartment model

A vessel cross section area

U cross-section-averaged velocity

C cross-section-averaged concentration

k scalar diffusivity

$\mathbb{K}$ diffusivity tensor

R vessel radius

ω concentration-velocity correlation coefficient

$\xi^{(\mathrm{B})}$ quantity ξ in bile

$\xi^{(\mathrm{H})}$ quantity ξ in hepatocytes

$\xi^{(\mathrm{S})}$ quantity ξ in blood

Double perfusion model

$H^{(\mathrm{B})}$ permeability in bile

$H^{(\mathrm{S})}$ permeability in blood

G compartment inter-permeability

H scalar permeability

$p^{(\mathrm{B})}$ pressure in bile

$P_{\mathrm{PV}}^{(\mathrm{B})}$ pressure in bile at the periportal end

$p^{(\mathrm{S})}$ pressure in blood

$P_{\mathrm{CV}}^{(\mathrm{S})}$ pressure in blood at the pericentral end

$P_{\mathrm{PV}}^{(\mathrm{S})}$ pressure in blood at the periportal end

Exchanges across interfaces

$c^{(\mathrm{comp})}$ complex concentration

$c^{(\mathrm{enz})}$ enzyme concentration

$c^{(\mathrm{prod})}$ product concentration

$c^{(\mathrm{sub})}$ substrate concentration

k_+ forward reaction rate constant

V_{max} maximum reaction rate

K_{m} Michaelis-Menten constant

k_- reverse reaction rate constant

Dimensionless numbers

Kn   Knudsen number

Ma   Mach number

Pe   Péclet number

Re   Reynolds number

Numerical solvers

`FVMStep` one step of the finite volume method solver

`RungeKuttaStep` one step of the Runge-Kutta solver

Δz space step

Δt time step

Abbreviations

ATP   adenosine triphosphate

BVP   boundary-value problem

CV   central vein

IBVP   initial-boundary-value problem

NTCP   sodium/taurocholate cotransporting polypeptide

ODE   ordinary differential equation

PV   portal vein

List of Figures

List of Tables

Contents

Introduction

Liver diseases have been displaying an increasing incidence in the human population in recent times. Namely, hepatocellular carcinoma rank fourth in mortality among cancers. To treat these diseases, a deep understanding of liver function is required. The complexity of processes involved and their interplay at many levels of organization favors approaches of systems medicine, where experiments, clinical data acquisition and computational modelling are integrated.

Most of the liver function is carried out inside *lobules* where drugs, toxins, and nutrients enter in blood coming from the intestine, penetrate into hepatic cells, where they possibly undergo various metabolic reactions, and are secreted into bile, which then transports them out of the organ (cf. Figure 1.1).

Computational models are able to verify or falsify hypothesized mechanisms occurring along this briefly described journey, and have already led to the identification of unrecognized mechanisms. These could then be used to propose new therapeutic strategies, for example by Ghallab et al. [2016]. More recently, using a similar approach, Vartak et al. [2021b] have revived the debate on mechanisms of bile transport in bile canaliculi, the smallest bile conduits in the liver.

Several modelling studies in recent years have treated flow and transport in liver micro-architecture. Boissier et al. [2021] have modelled micro-circulation in vascular networks of liver lobules, with an emphasis on the numerical simulation of fluorescent compound transport in these networks. However, these studies assume that the transport in blood is by pure advection. This is similar to work done by Dichamp et al. [2023], where in addition to flow and transport the model accounts for exchange with neighboring cells.

Vartak et al. [2021b], on the other hand, focused on transport in the bile canaliculi network, but did not consider the entire pathway of bile salts from liver blood capillaries (sinusoids), through hepatocytes, up to their excretion into bile canaliculi and eventually to bile ducts from where they are transported to the gallbladder.

Various components are necessary for a fully descriptive model at the level of liver tissue micro-architecture. The vessel tissue should be deformable and permeable, transport should include both advection and diffusion in both blood and bile, as well as exchanges across interfaces between blood and hepatocytes and hepatocytes and bile. Different exchange mechanisms and their relevance should be considered there. In general, a compound transported in liver micro-

architecture participates in multiple metabolic processes inside hepatocytes. Given the complexity of the full problem at hand, these requirements may make such a model computationally inefficient or even infeasible. To overcome this, various model reduction techniques can be applied, that partially depend on the nature of available data.

The simplest approach is to view the liver as a *well-mixed compartment* interacting with other organs and whole-body circulation via a *lumped parameter compartment model*, as demonstrated for example by Audebert and Vignon-Clementel [2018]. While this approach is computationally efficient, it neglects spatial variation of the organ behavior, which are of great significance in liver. While the fundamental idea behind modelling metabolic processes in hepatocytes is simple, and from a mathematical point of view reduces to a system of ODEs, in practice reduced models, which can be obtained in multiple ways under different assumptions, are almost always used. As far as flow is concerned, homogenization techniques are frequently used to derive a multiscale representation of the tissue microstructure, for example by Hodneland et al. [2019] in brain and by Rohan et al. [2021a] in liver.

Thesis Goals

The overall goal of this thesis is to derive and implement a proof-of concept compartment model of fluorescent marker transport in the blood – hepatocytes – bile system at the level of liver micro-architecture. The steps to achieve it are summarized below.

1. Situate the system of interest in a relevant physiological context. Identify key actors in the flow and transport of chemical compounds in the liver at the level of its micro-architecture.

2. Identify transport mechanisms inside the compartments of the blood – hepatocytes – bile system, as well as exchange mechanisms between these compartments.

3. Formulate general 3D governing equations for a mixture in sinusoids and bile canaliculi.

4. Derive a reduced 1D form of these equations along the vessel axis.

5. Formulate a model of exchanges across interfaces between the compartments in the blood – hepatocytes – bile system.

6. Use previous points to formulate the whole 1D-0D-1D compartment model of the system.

7. Implement the model numerically for a simple proof-of-concept geometry and interpret obtained results.

8. Discuss possible extensions of the model with the outlook of applying it to real-world experimental setups.

Thesis Outline

Chapter 1 introduces the physiological context of the studied system. We briefly describe liver structure and its function, placing emphasis on the journey of diverse chemical compounds of interest inside the liver lobule from blood to hepatocytes and subsequently to bile. Viable transport mechanisms across interfaces in this system are studied in further detail.

In Chapter 2, we derive the 1D-0D-1D compartment model for the blood – hepatocytes – bile system at the core of this thesis. We start by stating the assumptions made in the construction of the model. Next, we formulate the 3D governing equations for compound transport in blood and bile using concepts of mixture theory, and derive their 1D reduced forms. The strategy used in reducing the equations differs slightly from the one used in reference literature. We explain the difference as well as the reason for choosing an alternative method, and we suggest a modification of the established strategy that leads to results similar to those that we obtained. We then outline briefly the derivation of formulae for fluxes across the compartment interfaces, before finally presenting the complete compartment model for fluorescent compound transport.

Examples of results of the model are shown in Chapter 3, where we present its numerical implementation, briefly describe the solution algorithm, and provide prototypical interpretations of obtained results.

Before concluding, we discuss different aspects of presented work in Chapter 4. We review the modelling choices made throughout the thesis, and discuss possible extensions into more realistic settings and multiscale models. We then review critically the numerical methods used in the implementation, before finishing with an outline of future research and long-term goals for research in this direction.

Chapter 1

Physiology of Liver Function and Fluorescent Marker Transport

This chapter provides an overview of the physiological context of the model proposed in this work. Its aim is twofold – first, to motivate the construction of models like the one formulated later and show its possible practical applications; second, to briefly go through the liver structure and function in enough detail to justify and provide background for modelling assumptions made later on.

After the initial outline of the general structure and roles of the liver as an organ, we focus on its main structural element, the *liver lobule*. We describe its micro-architecture and how it pertains to the model proposed in the following chapter. Finally, we review the specifics of fluorescent marker transport mechanisms.

The majority of information stated here is adapted from the thesis by Boissier [2018] and the references therein. Sources are therefore explicitly cited only at points where the content deviates from that appearing in the aforementioned thesis.

1.1   Liver Organization and Function

Besides its important size in most relevant species, liver has a key role in whole-body regulation of such compounds as nutrients or toxins. Its main functions are *bile production* and *blood detoxification*. The former ensures transport of bile salts (e.g. cholesterol) out of the liver and into the rest of the body. The latter consists of transporting drugs, metabolites, and toxins from blood, possibly further modifying them inside the organ micro-architecture, before finally secreting them into bile. This mechanism also regulates concentrations of several key compounds on the single-organ as well as the whole-body level.

Any modifications or malfunctions of these mechanisms can induce liver pathologies. High concentrations of toxins and drugs in hepatocytes can lead to recoverable or permanent damage to cells and tissue, resulting in diseases ranging from fibrosis to liver tissue necrosis or cirrhosis, which can eventually develop into primary liver cancer.

Understanding the details of liver function mechanisms is clearly of utmost importance in both disease prevention and treatment. In this respect, accurate modelling of transport mechanisms inside liver plays a key role from the point of view of scientific and clinical applications.

Before discussing liver structure and organization, we start with a brief description of the "journey" of compounds such as drugs, toxins, or nutrients through liver tissue. Blood enters the liver through both the *portal vein* (PV) and the *hepatic artery*, the latter being rich in nutrients and similar compounds. These then travel through the vascular micro-architecture, possibly being taken up by surrounding cells and secreted into bile. They are then transported out of liver either in bile ducts leading to the gallbladder, or via the *central veins* (CV) in liver lobules (see below), which then lead to the inferior vena cava.

1.2 Liver Lobule

Structurally, liver is divided into several lobes (the exact numbers differ among species), each of them subdivided into structural units called *lobules*. Their shape is approximately hexagonal, although advances in liver microstructure segmentation via image recognition have contested this assumption and have revived the debate about structural classification of liver tissue (cf. Teutsch [2005]). Liver lobules contain namely *hepatocytes*, the cells responsible for the main part of liver function. These cells communicate with *sinusoids*, a special type of *blood capillaries* inside the lobules, and *bile canaliculi*, were they secrete bile along with the metabolized chemical compounds mentioned earlier.

The structural organization of liver is illustrated in Figure 1.1.[1] In the figure, we have marked the region of interest for our model in red, with the arrows showing the direction of compound transport. The exact mechanisms by which this transport occurs are discussed in the following section.

1.3 Transport Mechanisms

In the blood – hepatocytes – bile system, the three main transport mechanisms across interfaces are

- *active transport*, which consists of ATP molecules pulling the compounds in or out of the cells against the concentration gradient,

- *passive diffusion*, in which sufficiently hydrophobic molecules pass through cell membranes as a result of their concentration gradient,

- *facilitated diffusion*, where transport occurs as a result of the concentration gradient in a compound different to the compound of interest.

We now proceed to specify which of these mechanisms are relevant for each interface (cf. Schulze et al. [2019], Kamisako et al. [1999]). As can be seen in Figure 1.2, courtesy of van de Steeg et al. [2012], there are numerous possible modes of transport between the sinusoids, the hepatocytes, and the bile canaliculi, and their relative dominance depends heavily on the particular compounds transported. In this work, we concentrate mainly on transport of fluorescent tracers used in experiments on mice. This is due to the long-term goal of the developed model being to fit data from a specific experimental setup for mouse liver lobules. The

---

[1]The image was taken from `bioninja.com.au`.
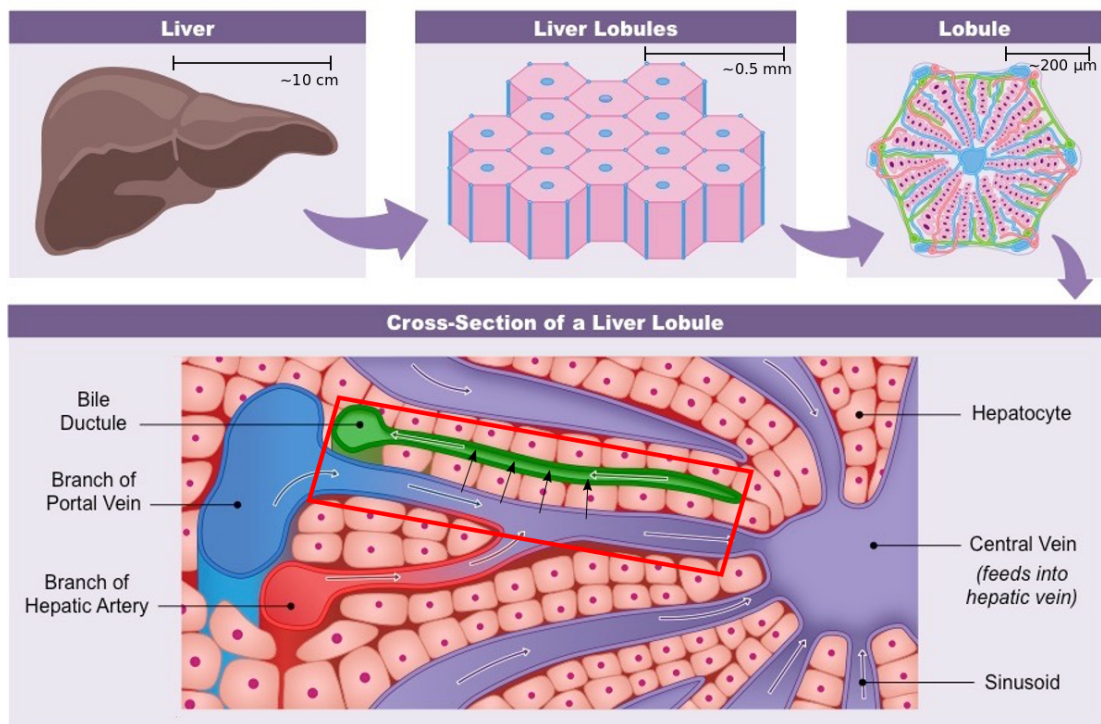
Figure 1.1: Liver structure classification – image taken from `bioninja.com.au`. The whole liver is first divided into several lobes, which are constituted by liver lobules – the main structural units of liver. In theory, these are assumed to have a hexagonal shape, although this has recently been contested (cf Teutsch [2005]). Inside the lobules, blood from the portal vein and the hepatic artery mixes, and diverse compounds are taken up from it by hepatocytes. These metabolize the compounds and secrete them into bile, which then transports them out of the lobule and eventually out of the organ.

discussion of transport mechanisms below will therefore be in some sense specific to these compounds.

At the time of writing, no exchange occurring between adjacent hepatocytes has been observed experimentally. Moreover, this exchange is not realistic even from a theoretical point of view, since the processes happening outside hepatocytes are much more efficient at compound clearance. We will therefore not consider the interfaces between hepatocytes in what follows.

It is also possible that the compound gets sequestered at some points of its journey through the blood – hepatocytes – bile system, i.e., it is stored and slowly leaks out. From an experimental point of view, there is little knowledge about this process, although, in theory, it would be possible in some parts of the system.
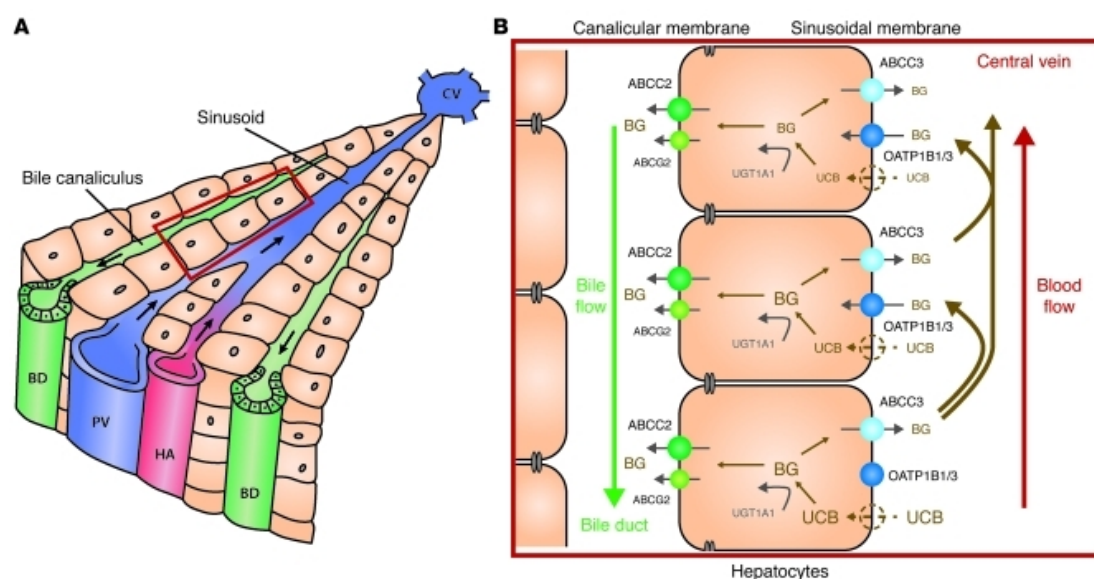
Figure 1.2: Transport mechanisms inside the liver lobule – image courtesy of van de Steeg et al. [2012]. There are multiple modes of transport across interfaces in the blood – hepatocytes – bile system. However, in the particular case of fluorescent tracer transport, the prevailing idea is that the compounds are taken up from blood via facilitated diffusion, and get in bile via active secretion (cf. Schulze et al. [2019], Kamisako et al. [1999]).

1.3.1   Blood-Hepatocyte Interface

First, according to current experimental results, no active transport occurs between the blood capillaries and hepatocytes. The largely prevalent portion of transport is due to *facilitated diffusion.* More specifically, energy from the NTCP sodium cation concentration gradient is used to transport the compound of interest from the blood into the hepatocytes. This mechanism could in theory be rate-limiting, although this has not been measured in real-world conditions thus far.

As for the transport by passive diffusion, while it cannot be completely excluded, it is expected to be very weak in presence of facilitated diffusion and has not been measured in practice.

1.3.2 Hepatocyte-Bile Interface

Contrary to the previous case, the transport between hepatocytes and bile canaliculi is almost always *active*. Different transporters are responsible for the exchange, and the secretion rates for the hepatocyte-bile interface are dictated by the particular combination of these transporters in the hepatocyte membrane.

1.3.3 Effect of Zonation

The experimentally observed anisotropy in transport properties along the PV-CV axis is mostly due to different amounts of transporters along the axis (cf. Tachikawa et al. [2018]). From a modelling point of view, these differences are relevant for the rate-limiting processes in the transport chain for each individual compound of interest. It is worth noting that the space-dependent characteristics need not be monotone along the PV-CV axis, and have a non-trivial experimental bias. For example, in experimental studies on mice, the compound is injected through the tail into the portal vein. The PV hepatocyte uptake tends to be very fast, inducing a concentration gradient in blood, which in turn necessarily induces zonation into the transport properties along the PV-CV axis.

Chapter Summary In this chapter, we have introduced the physiological context of the model at the core of this thesis. After a brief review of liver function and its structural organization, we have established the liver lobule as the structural unit of interest. In the liver lobule, chemical compounds are transported from blood in sinusoids through neighboring hepatocytes into bile canaliculi. Specifically, fluorescent tracers are taken up by hepatocytes via facilitated diffusion and then secreted into bile canaliculi by active transport. Exchange rates for both mechanisms can vary across different lobule regions. Equipped with this contextual information, we are ready to formulate a mathematical model of flow and transport in this system.

Chapter 2

Mathematical Modelling of Fluorescent Compound Transport

In view of the practical applications of liver function models presented in previous chapters, these have to be derived or postulated with great care for the sense and implications the assumptions have with respect to the biophysical reality. The following chapter attempts to describe a model of fluorescent tracer transport inside the liver lobule micro-architecture with these concerns in mind.

We start by formulating general equations for each part of the system, namely we state the balance laws in the blood capilary and the bile canaliculus in a general form and in 3D geometry. We then proceed with the derivation of a general strategy of reducing the 3D equations into 1D, taking into account the domain geometry. Finally, we use this strategy to derive governing equations for flow and transport in the reduced 1D setting. We comment briefly on alternative approaches to the model reduction, discussing their pitfalls and applicability.

After formulating equations for flow and transport, we continue with a review of mathematical models of compound transport across interfaces, and discuss assumptions made in deriving them.

We conclude by presenting the full compartment model of the blood – hepatocytes – bile system constructed from the previously presented elements.

2.1 3D Model Description

We first present a reasonably general approach to modelling flow and transport of fluorescent tracers in the system. Motivated by its real-world properties, we formulate the governing equations in the framework of 3D continuum mixture theory.

2.1.1 General Modelling Assumptions

Schematically, the system we are modelling consists of three interacting parts:

1. In the *sinusoids* of *blood capilaries*, the blood from the portal vein and the hepatic artery mixes and transports any of the compounds present towards the central vein at the center of the lobule. Here, we make the first modelling assumption by *neglecting hepatic arterial blood flow*. As [Boissier,

2018, Section 1.1.1] mentions, hepatic arterial blood flow accounts for $20-30\%$ of total blood inflow. Moreover, it is the blood from the portal vein that is rich in nutrients and other compounds, the transport of which we want to model.

Apart from blood flow and compound transport, the sinusoid walls can *deform* (cf. Greuter and Shah [2016]) and provide a means of *communication with the outer environment*, more specifically with hepatocytes.

2. The *hepatocytes* take up compounds transported by blood from the portal vein (and possibly also from the hepatic artery). Inside the cells, compounds can be metabolized in numerous ways, which we will not treat in detail at the moment. Products of the reactions are then secreted into bile canaliculi.

3. *Bile canaliculi* ensure bile formation and transport of metabolized compounds into the bile duct network and eventually out of the liver. Like sinusoids, they should also be modelled as *compliant vessels.*

As for the exact nature of bile formation and flow, it has been the subject of a lively debate even recently. As outlined in the review paper by Vartak et al. [2021a], bile transport in liver has historically been described by the *osmotic concept*, with bile flowing into the canaliculi towards the bile ducts, in the direction opposite to the sinusoidal blood flow. This concept was sufficient to explain clearance characteristics of many choleretic compounds excreted in bile. However, due to the small size of bile canaliculi, it was impossible to observe or quantify this process directly.

Recent advances in imaging techniques, however, have allowed for direct flux analysis in bile canaliculi. This analysis suggests that the flow of molecules in bile is *diffusion-dominated* and that *canalicular flow is negligible.* For the interlobular ducts, *diffusion is augmented by flow.*

Currently, there are two opposing theories on this matter:

1. The first postulates an *osmotically driven flow* inside the canaliculi. Bile acids along with other solutes have a strong osmotic potential and therefore draw water from the hepatocytes into bile canaliculi. Since the canalicular network is closed at the pericentral side, there is a directed flow towards the periportal bile duct. This was historically the first concept of bile transport and although it explains several macroscopic measurements, it was never observed or measured directly. Among others, Meyer et al. [2017] is a prime example of this theory.

2. Recent advances in imaging techniques have allowed for direct flux analysis in bile canaliculi. This analysis suggests that bile transport in the canaliculi is closer to a *diffusion in a stagnant fluid,* and that fluid flow is evident only in the ducts. The distinction between the two opposing theories is important for metabolism of certain compounds and for liver disease therapy. This concept is due to Vartak et al. [2021b].

From the mathematical modelling point of view, this context implies that we should take special care in deriving equations for bile transport, ideally accounting for transport both by advection and by diffusion. Incidentally, effects of diffusion

in blood can also be non-negligible, therefore it is of interest to include this in our model, too.

2.1.2 Mixture Theory Formulation

The main aim is to model transport of a fluorescent tracer injected into the cardiovascular system. Thus, we are effectively describing a mixture of blood plasma and the fluid containing the tracer. Following the mixture theory outline by [Hutter and Jöhnk, 2004, Chapter 7], we have decided to model the blood and bile parts of the systems as *Class I multi-component* (in the simplest case two-component, the two components being blood plasma or bile and fluorescent tracer fluid) *mixtures*. This means in particular that we are prescribing only the mass balance equations component-wise. The linear momentum balance, as well as eventually balances of energy and entropy are formulated for the mixture as a whole. This is motivated by the relative simplicity of description for Class I mixtures, and is justified by reasonably similar rheological properties of the contrast fluid and the blood plasma/bile. We will make a brief remark on constitutive relations relevant to the studied system at the end of this section.

Before formulating the governing equations in each compartment, we start by recalling the key concepts of mixture theory used in what follows. The starting point of our description of mixtures is the *coexistence assumption*, simply stating that all components of the mixture are present in all material points. We use *partial densities* ρ_α, $\alpha = 1, \ldots, N$ to represent the proportions of respective components in each material point. This means that the mass $\mathcal{M}_\alpha(\mathcal{V})$ of the α-th component contained inside a control volume $\mathcal{V}$ can be expressed as $\mathcal{M}_\alpha(\mathcal{V}) = \int_\mathcal{V} \rho_\alpha \, dV$. The density ρ of the whole mixture is defined in an analogous manner as $\mathcal{M}(\mathcal{V}) = \int_\mathcal{V} \rho \, dV$.

Next, we define *component concentration* c_α as the mass fraction of the component, i.e.,

$$c_\alpha := \frac{\rho_\alpha}{\rho}. \tag{2.1}$$

This definition implies that c_α is dimensionless and always less than or equal to 1. Moreover, under the reasonable assumption of *mass additivity*, we have

$$\sum_{\alpha=1}^N \rho_\alpha = \rho \implies \sum_{\alpha=1}^N c_\alpha = 1. \tag{2.2}$$

While the presented definition of concentration is convenient from a theoretical point of view, in real measurements we usually encounter other notions of concentration, namely *molar concentration*, measured usually in $\mathrm{mol\,cm^{-3}}$, and the *mass concentration*, measured in $\mathrm{g\,cm^{-3}}$. The latter actually coincides with the above defined partial density ρ_α. As for molar concentration, it can be easily recovered using mass fraction concentration, since

$$n_\alpha(\mathcal{V}) = \int_\mathcal{V} c_\alpha^{(\mathrm{molar})} \, dV \implies c_\alpha^{(\mathrm{molar})} = \frac{\rho c_\alpha}{N_\mathrm{A} M_\alpha}, \tag{2.3}$$

where $n_\alpha(\mathcal{V})$ denotes the number of moles of the α-th component in the control volume $\mathcal{V}$, M_α is the molar mass of the α-th component, and N_A is the Avogadro's constant.

With all the relevant component-wise quantities properly defined, we can proceed to stating the balance laws. Since our model describes mechanical phenomena without considering thermo-mechanical coupling[1], we will not formulate balances of energy and entropy. As for the rest,

- the *mass balance* for separate components of the mixture can be rewritten into the form

$$\frac{\partial \rho}{\partial t} + \mathrm{div}\,(\rho \boldsymbol{v}) = 0, \tag{2.4}$$

$$\rho \left(\frac{\partial c_\alpha}{\partial t} + \boldsymbol{v} \cdot \nabla c_\alpha \right) + \mathrm{div}\,\boldsymbol{j}_\alpha = m_\alpha, \quad \alpha = 1, \ldots, N, \tag{2.5}$$

  with $\boldsymbol{v}$ denoting the whole-mixture velocity, $\boldsymbol{j}_\alpha$ the diffusive flux of the α-th component, and m_α its production, e.g., due to chemical reactions;

- the *linear momentum balance* is prescribed for the whole mixture and has the classic form

$$\frac{\partial}{\partial t}(\rho \boldsymbol{v}) + \mathrm{div}\,(\rho \boldsymbol{v} \otimes \boldsymbol{v}) = \mathrm{div}\,\mathbb{T} + \rho \boldsymbol{b}, \tag{2.6}$$

  where $\mathbb{T}$ is the Cauchy stress tensor and $\boldsymbol{b}$ is the body force density;

- the *angular momentum balance* reduces to the symmetry condition for the Cauchy stress tensor, i.e., $\mathbb{T} = \mathbb{T}^T$. In general, if the components of the mixture exhibit intrinsic rotational behavior (e.g. in the form of spins), we would have to include additional equations in our model. However, we consider non-polar mixtures only in here, primarily for the sake of simplicity.

The above equations are relatively general, and can describe flow and transport of multiple components in blood as well as in bile. Naturally, closure relations have to be provided in each case by prescribing constitutive relations for the Cauchy stress and the diffusive fluxes.

An obvious first choice for blood and bile rheology could be the *incompressible Newtonian fluid*, with the Cauchy stress tensor given by

$$\mathbb{T} := -p\mathbb{I} + \eta \left(\nabla \boldsymbol{v} + (\nabla \boldsymbol{v})^T \right), \tag{2.7}$$

where p is the pressure and η the fluid viscosity. While an argument could be made for bile fitting the model assumptions for this constitutive relation, the heterogeneous nature of blood plasma suggests the need for a more complex rheological description. In particular, the red blood cells influence the flow properties of blood, especially in small veins and capillaries. This phenomena is called the Fahraeus-Linqvist effect. The simplest way of taking it into account is by introducing *apparent* viscosity into Equation (2.7) to replace the actual blood

---

[1]This is clearly a bold assumption, since apart from the flow we are also modelling chemical exchanges between blood, hepatocytes, and bile, as well as possible metabolic processes inside hepatocytes. The thermodynamic aspect of these processes is surely non-trivial. However, for the sake of simplicity, this aspect is neglected here.

plasma viscosity η. Secomb and Pries [2013] proposed an empirical formula for effective blood viscosity that reads

$$\eta_{\text{eff}} = \eta \left[1 + (\eta_{45} - 1) \frac{(1 - H_{\text{D}})^C - 1}{(1 - 0.45)^C - 1} \left(\frac{2R}{2R - 1.1} \right)^2 \right] \left(\frac{2R}{2R - 1.1} \right)^2, \qquad (2.8)$$

where

$$C = \left(0.8 + \text{e}^{-0.15R} \right) \left(-1 + \left(1 + 10^{-11} R^{12} \right)^{-1} \right) + \left(1 + 10^{-11} R^{12} \right)^{-1},$$

$$\eta_{45} = 6\text{e}^{-0.17R} + +3.2 - 2.44\text{e}^{-0.06(2R)^{0.645}},$$

R is the vessel radius, and H_{D} is the discharge hermatocrit. This formula captures experimentally observed effects of red blood cells on blood flow properties for vessels of different radii.

In the compartment model presented below, we put emphasis mainly on transport, taking the already computed flow field as an input to the model. We will therefore not discuss the issue of rheology further, the above example serving as an illustration of a possible approach.

2.2   Model Reduction

In models of flow in blood vessels (and by extension in bile canaliculi), it is often impractical to compute full 3D problems, given the complexity of vascular networks. The simplest model reduction technique lies in reformulating the 3D governing equations as 1D equations for cross-section-averaged quantities in the axial direction of the vessel. We will now illustrate the general strategy behind this technique, and then apply it to particular balance laws. While the reference on this subject seems to be the textbook by [Formaggia et al., 2009, Chapter 10], the strategy we present here is slightly different from the one presented therein. We will comment on these differences and their implications in Section 2.2.3.

2.2.1   Reduction of a General Balance Law

Consider a fluid flowing in an axially symmetric tube with a deformable wall. This means that its radius R can be space- and time-dependent, i.e., $R = R(t, z)$, z being the axial coordinate. The situation is illustrated in Figure 2.1. We further consider a control volume $\mathcal{V}_\delta(t)$ that has special form illustrated in Figure 2.1. We assume that this control volume is *material*. More specifically, we assume that the cross-section parts of the boundary Σ_-, Σ_+ move with the fluid, and the wall part of the boundary Γ_δ moves with the vessel wall. If $\boldsymbol{v}$ is the fluid velocity, $\boldsymbol{v}_{\text{w}}$ is the velocity of the vessel wall, and $\boldsymbol{v}_{\text{b}}$ the boundary velocity, we can write this as

$$\boldsymbol{v}_{\text{b}}|_{\Sigma_-} = \boldsymbol{v}|_{\Sigma_-}, \quad \boldsymbol{v}_{\text{b}}|_{\Sigma_+} = \boldsymbol{v}|_{\Sigma_+}, \quad \boldsymbol{v}_{\text{b}}|_{\Gamma_\delta} = \boldsymbol{v}_{\text{w}}. \qquad (2.9)$$

Before going further, we make a brief note of the notation used in the derivation. In what follows, $\text{d}V$, $\text{d}S$, $\text{d}\gamma$ denote volume, surface, and contour measures, respectively. The unit normal to the boundary (surface boundary for volumes, contour boundary for surfaces) will be denoted $\boldsymbol{n}$ with subscript of the corresponding boundary in case of possible ambiguity.
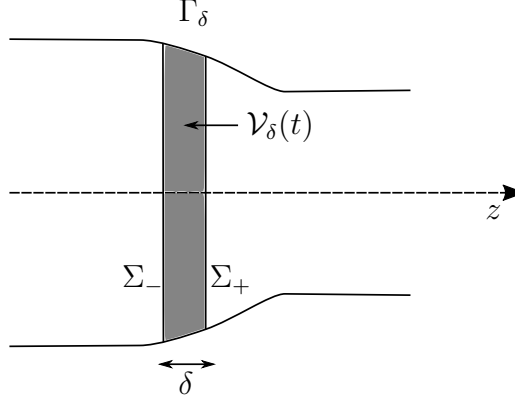
Figure 2.1: Vessel geometry and control volume.

The integral form of a general balance law for a quantity ψ over this control volume reads

$$\int_{\mathcal{V}_\delta(t)} \frac{\partial \psi}{\partial t}\, \mathrm{d}V + \int_{\partial \mathcal{V}_\delta(t)} \psi \boldsymbol{v}_\mathrm{b} \cdot \boldsymbol{n}\, \mathrm{d}S = \int_{\partial \mathcal{V}_\delta(t)} \boldsymbol{j}^{(\psi)} \cdot \boldsymbol{n}\, \mathrm{d}S + \int_{\mathcal{V}_\delta(t)} r^{(\psi)}\, \mathrm{d}V, \qquad (2.10)$$

where $\boldsymbol{j}^{(\psi)}$ represents the fluxes of ψ and $r^{(\psi)}$ the volume source terms (including production, supply, and interaction).

Next, we study of the limit of Equation (2.10) multiplied by $1/\delta$ as $\delta \to 0$, proceeding term by term.

We start with the term containing $\frac{\partial \psi}{\partial t}$, where we can write

$$\frac{1}{\delta} \int_{\mathcal{V}_\delta(t)} \frac{\partial \psi}{\partial t}\, \mathrm{d}V = \frac{1}{\delta} \int_z^{z+\delta} \left(\int_{\Sigma(t,\hat{z})} \frac{\partial \psi}{\partial t}\, \mathrm{d}S \right) \mathrm{d}\hat{z}$$

$$= \frac{1}{\delta} \int_z^{z+\delta} \left(\frac{\partial}{\partial t}(A\overline{\psi}) - \int_{\partial\Sigma(t,\hat{z})} \psi \boldsymbol{v}_\mathrm{w} \cdot \boldsymbol{n}_{\partial\Sigma}\, \mathrm{d}\gamma \right) \mathrm{d}\hat{z}$$

$$\xrightarrow{\delta \to 0} \frac{\partial}{\partial t}(A\overline{\psi}) - \int_{\partial\Sigma(t,z)} \psi \boldsymbol{v}_\mathrm{w} \cdot \boldsymbol{n}_{\partial\Sigma}\, \mathrm{d}\gamma,$$

where we have used the 2D version of the Reynolds transport theorem for the cross-section

$$\frac{\partial}{\partial t} \int_{\Sigma(t)} \psi\, \mathrm{d}S = \int_{\Sigma(t)} \frac{\partial \psi}{\partial t}\, \mathrm{d}S + \int_{\partial\Sigma(t)} \psi \boldsymbol{v}_\mathrm{b} \cdot \boldsymbol{n}_{\partial\Sigma}\, \mathrm{d}\gamma,$$

along with assumptions (2.9) and the definition

$$\overline{\psi} := \frac{1}{A} \int_\Sigma \psi\, \mathrm{d}S, \quad \text{where} \quad A := |\Sigma|$$

for the cross-section average of the quantity ψ.

We follow by treating the surface integral term on the left-hand side of Equation

(2.10) as follows:

$$\frac{1}{\delta}\int_{\partial\mathcal{V}_\delta(t)}\psi\boldsymbol{v}_{\mathrm{b}}\cdot\boldsymbol{n}\,\mathrm{d}S=\frac{1}{\delta}\left(\begin{array}{c}\int_{\Sigma_-}\psi\boldsymbol{v}\cdot\boldsymbol{n}_{\Sigma_-}\,\mathrm{d}S\\[4pt]+\int_{\Sigma_+}\psi\boldsymbol{v}\cdot\boldsymbol{n}_{\Sigma_+}\,\mathrm{d}S\\[4pt]+\int_{\Gamma_\delta}\psi\boldsymbol{v}_{\mathrm{w}}\cdot\boldsymbol{n}_{\Gamma_\delta}\,\mathrm{d}S\end{array}\right)$$

$$=\left\{\begin{array}{c}\frac{1}{\delta}\left(\int_{\Sigma_+}\psi v_z\,\mathrm{d}S-\int_{\Sigma_-}\psi v_z\,\mathrm{d}S\right)\\[6pt]+\frac{1}{\delta}\int_z^{z+\delta}\int_{\partial\Sigma(t,\hat{z})}\frac{\psi\boldsymbol{v}_{\mathrm{w}}\cdot\boldsymbol{n}_{\Gamma_\delta}}{\cos\beta}\,\mathrm{d}\gamma\,\mathrm{d}\hat{z}\end{array}\right\}$$

$$\xrightarrow{\delta\to 0}\frac{\partial}{\partial z}(A\overline{\psi v_z})+\int_{\partial\Sigma(t,z)}\frac{\psi\boldsymbol{v}_{\mathrm{w}}\cdot\boldsymbol{n}_{\Gamma_\delta}}{\cos\beta}\,\mathrm{d}\gamma.$$

Since we consider possibly varying vessel radius, we need to include a $(\cos\beta)^{-1}$ factor in the contour integration, where β is the angle between the two normals $\boldsymbol{n}_{\partial\Sigma}$ and $\boldsymbol{n}_{\Gamma_\delta}$, as shown in Figure 2.2.

The volume integral term on the right-hand side of Equation (2.10) can be rewritten in a straightforward manner as

$$\frac{1}{\delta}\int_{\mathcal{V}_\delta(t)}r^{(\psi)}\,\mathrm{d}V=\frac{1}{\delta}\int_z^{z+\delta}\left(\int_{\Sigma(t,\hat{z})}r^{(\psi)}\,\mathrm{d}S\right)\mathrm{d}\hat{z}\xrightarrow{\delta\to 0}A\overline{r^{(\psi)}}.$$

As for the flux term on the right-hand side of Equation (2.10), we proceed analogously to the surface integral on the left-hand side, writing

$$\frac{1}{\delta}\int_{\partial\mathcal{V}_\delta(t)}\boldsymbol{j}^{(\psi)}\cdot\boldsymbol{n}\,\mathrm{d}S=\frac{1}{\delta}\left(\begin{array}{c}\int_{\Sigma_-}\boldsymbol{j}^{(\psi)}\cdot\boldsymbol{n}_{\Sigma_-}\,\mathrm{d}S\\[4pt]+\int_{\Sigma_+}\boldsymbol{j}^{(\psi)}\cdot\boldsymbol{n}_{\Sigma_+}\,\mathrm{d}S\\[4pt]+\int_{\Gamma_\delta}\boldsymbol{j}^{(\psi)}\cdot\boldsymbol{n}_{\Gamma_\delta}\,\mathrm{d}S\end{array}\right)$$

$$=\left\{\begin{array}{c}\frac{1}{\delta}\left(\int_{\Sigma_+}j_z^{(\psi)}\,\mathrm{d}S-\int_{\Sigma_-}j_z^{(\psi)}\,\mathrm{d}S\right)\\[6pt]+\frac{1}{\delta}\int_z^{z+\delta}\int_{\partial\Sigma(t,\hat{z})}\frac{\boldsymbol{j}^{(\psi)}\cdot\boldsymbol{n}_{\Gamma_\delta}}{\cos\beta}\,\mathrm{d}\gamma\,\mathrm{d}\hat{z}\end{array}\right\}$$

$$\xrightarrow{\delta\to 0}\frac{\partial}{\partial z}(A\overline{j_z^{(\psi)}})+\int_{\partial\Sigma(t,z)}\frac{\boldsymbol{j}^{(\psi)}\cdot\boldsymbol{n}_{\Gamma_\delta}}{\cos\beta}\,\mathrm{d}\gamma.$$

Putting these four terms back together results in

$$\frac{\partial}{\partial t}\left(A\overline{\psi}\right)+\frac{\partial}{\partial z}\left(A\overline{\psi v_z}\right)=\frac{\partial}{\partial z}\left(A\overline{j_z^{(\psi)}}\right)+J^{(\psi)}+A\overline{r^{(\psi)}},\qquad(2.11)$$

where we have defined

$$J^{(\psi)}:=\int_{\partial\Sigma(t,z)}\frac{\boldsymbol{j}^{(\psi)}\cdot\boldsymbol{n}_{\Gamma_\delta}}{\cos\beta}-\frac{\psi\boldsymbol{v}_{\mathrm{w}}\cdot\boldsymbol{n}_{\Gamma_\delta}}{\cos\beta}+\psi\boldsymbol{v}_{\mathrm{w}}\cdot\boldsymbol{n}_{\partial\Sigma}\,\mathrm{d}\gamma.$$

The above term represents eventual fluxes across the boundary, and its exact form is dictated by the boundary conditions of the 3D problem.

This is the sought after 1D reduction of the general balance law. It essentially states that the reduced governing equation has a form of a balance law for a 1D continuum with averaged quantities multiplied by the cross-section area, with an additional flux term representing exchanges with external media.
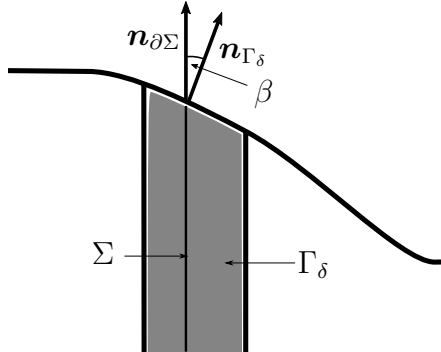
Figure 2.2: Different normals at the vessel boundary.

2.2.2 One-dimensional Balance Laws

In the following, we derive particular balance laws for mass, linear momentum, and component concentration by substituting appropriate quantities for ψ in Equation (2.11).

Mass Balance

In the usual 3D setting, the mass balance equation is obtained by substituting the density ρ into the general form of the balance law (cf. Equation (2.4)). In this case, however, we take a slightly different approach and set $\psi \equiv 1$. Mass conservation implies $r^{(\psi)} \equiv 0$ and $\boldsymbol{j}^{(\psi)} \equiv \boldsymbol{0}$. The mass balance then reads

$$\frac{\partial A}{\partial t} + \frac{\partial}{\partial z}(A\overline{v_z}) = 0. \tag{2.12}$$

As we can see, this equation represents the balance of volume rather than the balance of mass. This is connected to the fact that in reduced models of blood flow, constant density is usually assumed.[2]

Momentum Balance

Following the constant density assumption, we seek the linear momentum balance by substituting $\psi := \boldsymbol{v}$ instead of the usual $\rho\boldsymbol{v}$ term from Equation (2.6). The volume source term represents body forces, i.e., $r^{(\psi)} := \boldsymbol{b}$, and the flux term accounts for surface stresses, i.e., $\boldsymbol{j}^{(\psi)} := \mathbb{T}$. Throughout the cross-section averaging procedure, all except z-components vanish due to symmetry, and the result is

$$\frac{\partial}{\partial t}\left(A\overline{v_z}\right) + \frac{\partial}{\partial z}\left(A\overline{v_z^2}\right) = \frac{\partial}{\partial z}\left(A\overline{\mathbb{T}_{zz}}\right) + J^{(v_z)} + A\overline{b_z}. \tag{2.13}$$

---

[2]This may seem as an oversimplification, given the complex internal structure of blood plasma. One possible argument justifying such simplification is that the quantity ρ in the equations represents a sort of *effective* density that takes into account the structure of the real fluid.

As mentioned above, the term $J^{(v_z)}$ follows from boundary conditions in the 3D setting. The simplest choice clearly corresponds to $J^{(v_z)} \equiv 0$.

Since the eventual aim is to solve the above equation for $\overline{v_z}$, we introduce the *Coriolis coefficient* $\alpha := \overline{v_z^2}/\overline{v_z}^2$ that is non-dimensional and depends on the velocity profile. For example, for a flat profile $\alpha = 1$, while for a parabolic profile $\alpha = 4/3$ (cf. [Formaggia et al., 2009, Chapter 10]).

In order for the linear momentum balance to be well-posed (or part of a well-posed system), constitutive relations have to be provided for the Cauchy stress tensor $\mathbb{T}$. Detailed discussion of appropriate constitutive relations for blood and bile is beyond the scope of this work, but we refer the reader to Formaggia et al. [2009] for a brief outline.

Equation for Concentration

By setting $\psi := c_\alpha$, $\alpha = 1, \ldots, N$, we aim to find the 1D analog of Equation (2.5). In general, $\boldsymbol{j}^{(c_\alpha)}$ represents the diffusive fluxes of individual mixture components, and $r^{(c_\alpha)}$ represents the reactions between the components. The exact nature of both quantities depends on the properties of the studied system. In our case, it is reasonable to assume (for both blood and bile) that no reactions occur inside the vessel, but there is nontrivial exchange across the vessel wall. This exchange will be represented by the J_α term in the governing equation. For the purposes of our model, we further assume that the diffusive fluxes are given by *Fick's law*, i.e., $\boldsymbol{j}^{(c_\alpha)} := -\mathbb{K}\nabla c_\alpha$. The symbol $\mathbb{K}$ denotes the diffusivity tensor, if the diffusion is isotropic, then the scalar diffusivity will be denoted k.

If we incorporate all the assumptions and substitute in the general 1D balance equation, we get

$$\frac{\partial}{\partial t}\left(A\overline{c_\alpha}\right) + \frac{\partial}{\partial z}\left(A\overline{c_\alpha v_z}\right) = \frac{\partial}{\partial z}\left(A\overline{\boldsymbol{e}_z \cdot \mathbb{K}_\alpha \nabla c_\alpha}\right) + J_\alpha.$$

Furthermore, if in analogy with the linear momentum balance we introduce the *velocity-concentration correlation coefficient* $\omega_\alpha := \overline{c_\alpha v_z}/\overline{c_\alpha}\,\overline{v_z}$, and for the sake of simplicity assume homogeneous isotropic diffusion, the equation for component concentration now reads

$$\frac{\partial}{\partial t}\left(A\overline{c_\alpha}\right) + \frac{\partial}{\partial z}\left(\omega_\alpha A\overline{c_\alpha}\,\overline{v_z}\right) - k_\alpha\frac{\partial^2}{\partial z^2}\left(A\overline{c_\alpha}\right) = J_\alpha. \qquad (2.14)$$

This is essentially an advection-diffusion-reaction equation for individual components of the mixture. It is exactly this equation that we will use, after specifying transport mechanisms contributing to J_α, to model transport in blood as well as in bile.

2.2.3 Alternative Model Reduction Approaches

The strategy for deriving 1D reduced governing equations from their 3D counterparts presented here is somewhat different from the one presented in [Formaggia et al., 2009, Chapter 10]. While in theory both strategies should lead to equivalent results, we have chosen this particular derivation namely for consistency in the treatment of the deformable vessel wall, and the way in which the spatial derivatives of cross-section-averaged quantities are obtained.

However, the governing equation for concentration formulated by [Formaggia et al., 2009, Equation (10.34)] differs considerably from Equation (2.14) above, the most striking difference being the absence of the 1D diffusion term in the version of Formaggia et al. [2009]. Although Formaggia et al. [2009] do not provide exact derivation assumptions, [D'Angelo, 2007, Section 2.2] derives the equation in detail. The detailed derivation reveals that the argument leading to the 1D diffusion term being neglected is dimensional. Indeed, if L is the length of the vessel and R_0 is its characteristic radius, then we can define non-dimensional variables

$$\hat{r} := \frac{r}{R_0}, \quad \hat{z} := \frac{z}{L}.$$

Next, we assume that $R_0/L =: \varepsilon \ll 1$. If we now rewrite the 3D Laplacian operator in non-dimensional variables and neglect terms quadratic in ε, we get

$$\begin{aligned}
\Delta_{\text{3D}} c &= \frac{1}{R_0^2 \hat{r}} \frac{\partial}{\partial \hat{r}} \left(\hat{r} \frac{\partial c}{\partial \hat{r}} \right) + \frac{1}{R_0^2 \hat{r}^2} \frac{\partial^2 c}{\partial \theta^2} + \frac{1}{L^2} \frac{\partial^2 c}{\partial \hat{z}^2} \\
&= \frac{1}{R_0^2} \left[\frac{1}{\hat{r}} \frac{\partial}{\partial \hat{r}} \left(\hat{r} \frac{\partial c}{\partial \hat{r}} \right) + \frac{1}{\hat{r}^2} \frac{\partial^2 c}{\partial \theta^2} + \varepsilon^2 \frac{\partial^2 c}{\partial \hat{z}^2} \right] \\
&\approx \frac{1}{R_0^2} \left[\frac{1}{\hat{r}} \frac{\partial}{\partial \hat{r}} \left(\hat{r} \frac{\partial c}{\partial \hat{r}} \right) + \frac{1}{\hat{r}^2} \frac{\partial^2 c}{\partial \theta^2} \right] \\
&= \frac{1}{r} \frac{\partial}{\partial r} \left(r \frac{\partial c}{\partial r} \right) + \frac{1}{r^2} \frac{\partial^2 c}{\partial \theta^2} \\
&= \Delta_{\text{2D}} c,
\end{aligned}$$

where we have denoted the 2D and 3D Laplacian operators by the respective subscripts. If we compare this with the derivation of the governing equation for concentration, in particular the manipulations involving the flux term, we can see that this train of thought would indeed lead to neglecting the 1D diffusion term in the final equation.

Despite appearing innocent, the above approximation has its pitfalls. The main issue lies in the fact that the term quadratic in ε is further multiplied by $1/R_0^2$. Under the assumption that $R_0/L \ll 1$, R_0 is bound to be very small, e.g., of order of magnitude ε for L of order of magnitude 1, therefore making $1/R_0^2$ potentially very large. In this situation, even a perturbation of order ε^2 can be too important to be neglected. In the derivation of the governing equation for concentrations above, we have avoided such arguments altogether, and the above discussion shows yet another reason for choosing an alternative strategy.

Nevertheless, the scaling argument presented above can be used to derive the reduced 1D equation for concentration with the diffusion term present, provided that it is exploited in a slightly different manner. For the sake of generality, we can consider possibly non-isotropic diffusion and study the term $\text{div}\,(\mathbb{K}\nabla c)$ instead of $\Delta_{\text{3D}} c$. No generality is lost if we prescribe the diffusivity tensor in the form $\mathbb{K} := \text{diag}\,(k_r, 0, k_z)$.

If we start again by expressing this form of the diffusive term in cylindrical coordinates, this time omitting the angular derivatives due to assumed axial

symmetry, we find that

$$\text{div} (\mathbb{K}\nabla c) = \frac{1}{R_0^2 \hat{r}} \frac{\partial}{\partial \hat{r}} \left(\hat{r} k_r \frac{\partial c}{\partial \hat{r}} \right) + \frac{1}{L^2} \frac{\partial}{\partial \hat{z}} \left(k_z \frac{\partial c}{\partial \hat{z}} \right)$$

$$= \frac{1}{L^2} \left[\varepsilon^{-2} \frac{1}{\hat{r}} \frac{\partial}{\partial \hat{r}} \left(\hat{r} k_r \frac{\partial c}{\partial \hat{r}} \right) + \frac{\partial}{\partial \hat{z}} \left(k_z \frac{\partial c}{\partial \hat{z}} \right) \right]. \quad (2.15)$$

In the scaling argument, we take L to be of order 1 in comparison to R_0, which is of order ε. If we now look at the limit as $\varepsilon \to 0$ and require that the expression stays finite, it is clear that c cannot depend on r. This yields the sought after reduction of the 3D diffusion term to 1D diffusion along the z axis.

A similar argument can be developed for the advection term in the equation for concentration. In the 3D governing equation (2.5), advection is represented by the term $\boldsymbol{v} \cdot \nabla c$. The gradient in cylindrical coordinates, taking into account axial symmetry of the problem, reads

$$\nabla c = \frac{\partial c}{\partial r} \boldsymbol{e}_r + \frac{\partial c}{\partial z} \boldsymbol{e}_z = \frac{1}{L} \left(\varepsilon^{-1} \frac{\partial c}{\partial \hat{r}} \boldsymbol{e}_r + \frac{\partial c}{\partial \hat{z}} \boldsymbol{e}_z \right), \quad (2.16)$$

where we have used the scaling introduced above. Again, investigating the limit as $\varepsilon \to 0$, we find that if the term is to stay finite, then c cannot depend on r, and the gradient effectively reduces to a partial derivative along the z axis.

We can go one step further by comparing the scaling of radial terms in Equations (2.15) and (2.16). If we assume that the diffusivity tensor components scale as

$$k_z = k_0, \quad k_r = k_0 \varepsilon,$$

then, injecting this into Equation (2.15), we find that the radial terms in advection and diffusion scale with identical negative powers of ε. We can interpret this in the sense that these terms effectively "compensate". The above scaling could be justified for example if the diffusivities in specific directions depended linearly on the mean free path of compound microconstituents in those directions. However, even if such a hypothesis does not hold, the scaling argument leading to the reduced 1D form of the terms remains valid.

Note that the advection term thus obtained differs slightly from that in Equation (2.14), namely the velocity is kept outside the z-partial derivative in what is discussed here. However, the equivalence of the two terms can be shown via the mass balance (cf. Equation (2.12)).

2.3   Modelling Transport across Interfaces

The aim of the following section is to derive explicit forms of fluxes J_α appearing in Equation (2.14) and discuss the limits of validity of the proposed formulae. The content of this section is largely adapted from Chapter 2 of the reference textbook on the matter by Keener et al. [2009].

As discussed in Section 1.3, fluorescent compounds are transported across blood-hepatocyte and hepatocyte-bile interfaces notably via two mechanisms – *active transport* and *facilitated diffusion*. Before treating these mechanisms in detail, we recall for the purpose of further use in derivations the *law of mass action* used for determining reaction rates.

Consider two chemical compounds A and B reacting to form a single product C, written symbolically as

$$A + B \xrightleftharpoons[k_-]{k_+} C, \tag{2.17}$$

where k_+ and k_- are reaction-specific rate constants, and the double arrow indicates that the reaction in general happens in both directions, one defined as *forward* (corresponding to k_+) and other as *reverse* (corresponding to k_-). The definitions of the two directions follow from thermodynamic properties of the reaction and will not be discussed further here.

The law of mass action states that the rate of the chemical reaction (2.17), i.e., the rate of change in product concentration, is given by

$$\frac{\mathrm{d}c_{\mathrm{C}}}{\mathrm{d}t} = k_+ c_{\mathrm{A}} c_{\mathrm{B}} - k_- c_{\mathrm{C}}, \tag{2.18}$$

where c_{A}, c_{B}, c_{C} are concentrations of compounds A, B, C respectively. Despite being called a law, Equation (2.18) presents rather a useful model applicable to many situations. In particular, this model can be used, along with scaling considerations, to derive models for more complicated chemical processes.

2.3.1 Active Transport

When we say that a compound is taken up or secreted actively, we generally mean that it undergoes an enzymatic reaction of the form

$$\text{substrate} + \text{enzyme} \xrightleftharpoons[k_{-1}]{k_{+1}} \text{complex} \xrightarrow{k_2} \text{product} + \text{enzyme},$$

where the compound has the role of both substrate and product, and it is the complex that ensures the transport. If we denote the substrate, enzyme, complex, and product concentration by $c^{(\mathrm{sub})}$, $c^{(\mathrm{enz})}$, $c^{(\mathrm{comp})}$, and $c^{(\mathrm{prod})}$, respectively, then the law of mass action for this reaction chain reads

$$\begin{cases} \dfrac{\mathrm{d}c^{(\mathrm{sub})}}{\mathrm{d}t} = k_{-1} c^{(\mathrm{comp})} - k_{+1} c^{(\mathrm{sub})} c^{(\mathrm{enz})}, \\[2mm] \dfrac{\mathrm{d}c^{(\mathrm{enz})}}{\mathrm{d}t} = (k_{-1} + k_2) c^{(\mathrm{comp})} - k_{+1} c^{(\mathrm{sub})} c^{(\mathrm{enz})}, \\[2mm] \dfrac{\mathrm{d}c^{(\mathrm{comp})}}{\mathrm{d}t} = k_{+1} c^{(\mathrm{sub})} c^{(\mathrm{enz})} - (k_{-1} + k_2) c^{(\mathrm{comp})}, \\[2mm] \dfrac{\mathrm{d}c^{(\mathrm{prod})}}{\mathrm{d}t} = k_2 c^{(\mathrm{comp})}. \end{cases} \tag{2.19}$$

Since the above system is impractical to be fully solved, we reduce it under the *quasi-steady-state approximation*, i.e., assuming that the rates of formation and breakdown of the complex are essentially equal, and therefore $\frac{\mathrm{d}c^{(\mathrm{comp})}}{\mathrm{d}t} \approx 0$. Next, we introduce dimensionless variables

$$\sigma := \frac{c^{(\mathrm{sub})}}{c_0^{(\mathrm{sub})}}, \quad \xi := \frac{c^{(\mathrm{comp})}}{e_0}, \quad \tau := k_{+1} e_0 t,$$

$$\kappa := \frac{k_{-1} + k_2}{k_{+1} + c_0^{(\mathrm{sub})}}, \quad \varepsilon := \frac{e_0}{c_0^{(\mathrm{sub})}}, \quad \alpha := \frac{k_{-1}}{k_{+1} c_0^{(\mathrm{sub})}},$$

where $c_0^{(\text{sub})}$ is the characteristic substrate concentration and e_0 is the total amount of enzyme. Rewriting the system (2.19) using these variables, as well as assuming quasi-steady state, yields

$$\frac{\mathrm{d}\sigma}{\mathrm{d}\tau} = -\sigma + \xi(\sigma + \alpha), \quad \frac{\mathrm{d}\xi}{\mathrm{d}\tau} = \varepsilon^{-1}\left(\sigma - \xi(\sigma - \kappa)\right).$$

In practice, the concentration of enzymes needed to catalyze a reaction is considerably (i.e. orders of magnitude) lower than that of the substrate, which implies that $\varepsilon \ll 1$. Similarly to Section 2.2.3, we can investigate the limit as $\varepsilon \to 0$ and require that the right-hand side of the corresponding equation be well-defined, which leads to

$$\xi = \frac{\sigma}{\sigma + \kappa}.$$

Injecting this bc into dimensionless equations, and then going back to regular variables, we obtain the expression of *Michaelis-Menten kinetics* for enzymatic reactions

$$\frac{\mathrm{d}c^{(\text{prod})}}{\mathrm{d}t} = -\frac{\mathrm{d}c^{(\text{sub})}}{\mathrm{d}t} = \frac{V_{\max}c^{(\text{sub})}}{K_{\mathrm{m}} + c^{(\text{sub})}}. \tag{2.20}$$

The symbols $V_{\max}$, K_{m} denote the *maximal reaction rate* and the *Michaelis-Menten constant*, respectively.

It is worth noting that Michaelis-Menten kinetics have two characteristic regimes:

- the *linear regime* can be considered if $c^{(\text{sub})} \ll K_{\mathrm{m}}$, in which case we can approximately rewrite Equation (2.20) into the form

$$\frac{\mathrm{d}c^{(\text{prod})}}{\mathrm{d}t} = \frac{V_{\max}}{K_{\mathrm{m}}}c^{(\text{sub})};$$

- the *saturated regime*, which corresponds to $c^{(\text{sub})} \gg K_{\mathrm{m}}$, and where Equation (2.20) is approximated by

$$\frac{\mathrm{d}c^{(\text{prod})}}{\mathrm{d}t} = V_{\max}.$$

2.3.2 Facilitated Diffusion

The idea behind facilitated diffusion is that a compound that would normally diffuse relatively slowly across a membrane will have its diffusion rate enhanced significantly by entering an enzymatic reaction, the product of which is also diffusing across the membrane. Since the derivation of the flux for facilitated diffusion (demonstrated by Keener et al. [2009]) is slightly non-trivial, especially in terms of accepted hypotheses on the system, we go through it in detail here.

The reaction scheme considered here is

$$\text{substrate} + \text{enzyme} \underset{k_-}{\overset{k_+}{\rightleftharpoons}} \text{product}.$$

We model the reaction in a 1D continuum along the coordinate $x \in (0, L)$ by a system of *diffusion-reaction* equations

$$\frac{\partial c^{(\mathrm{sub})}}{\partial t} - D_{\mathrm{s}} \frac{\partial^2 c^{(\mathrm{sub})}}{\partial x^2} = -k_+ c^{(\mathrm{sub})} c^{(\mathrm{enz})} + k_- c^{(\mathrm{prod})}, \qquad (2.21)$$

$$\frac{\partial c^{(\mathrm{enz})}}{\partial t} - D_{\mathrm{e}} \frac{\partial^2 c^{(\mathrm{enz})}}{\partial x^2} = -k_+ c^{(\mathrm{sub})} c^{(\mathrm{enz})} + k_- c^{(\mathrm{prod})}, \qquad (2.22)$$

$$\frac{\partial c^{(\mathrm{prod})}}{\partial t} - D_{\mathrm{p}} \frac{\partial^2 c^{(\mathrm{prod})}}{\partial x^2} = k_+ c^{(\mathrm{sub})} c^{(\mathrm{enz})} - k_- c^{(\mathrm{prod})}, \qquad (2.23)$$

where $c^{(\mathrm{sub})}$, $c^{(\mathrm{enz})}$, $c^{(\mathrm{prod})}$ denote the concentrations of the substrate, the enzyme, and the product respectively, and D_i, $i = \mathrm{s}, \mathrm{e}, \mathrm{p}$ are the corresponding diffusion coefficients. Since the product is assumed to be similar in mass and structure to the enzyme, we take $D_{\mathrm{p}} \approx D_{\mathrm{e}}$ in the following.

Under the hypothesis that the total amount of enzyme is conserved in the reaction, we have $c^{(\mathrm{enz})} + c^{(\mathrm{prod})} = \mathrm{const.} =: c_{\mathrm{e}}$ at steady state. This makes Equation (2.22) redundant, and Equations (2.21) and (2.23) further reduce to

$$D_{\mathrm{s}} \frac{\partial^2 c^{(\mathrm{sub})}}{\partial x^2} + D_{\mathrm{e}} \frac{\partial^2 c^{(\mathrm{prod})}}{\partial x^2} = 0,$$

which yields immediately upon integration

$$D_{\mathrm{s}} \frac{\partial c^{(\mathrm{sub})}}{\partial x} + D_{\mathrm{e}} \frac{\partial c^{(\mathrm{prod})}}{\partial x} = \mathrm{const.} =: -J,$$

where J is the *facilitated diffusion flux*. Integrating this expression once again along the 1D continuum $(0, L)$ leads to

$$J = D_{\mathrm{s}} \frac{c^{(\mathrm{sub})}\big|_{x=0} - c^{(\mathrm{sub})}\big|_{x=L}}{L} + D_{\mathrm{e}} \frac{c^{(\mathrm{prod})}\big|_{x=0} - c^{(\mathrm{prod})}\big|_{x=L}}{L}. \qquad (2.24)$$

The interpretation of this equation is trivial, since it essentially states that the total diffusive flux of the compound of interest is composed of the diffusion of the compound alone, enhanced by the diffusion of the product of the reaction between the compound and the corresponding enzyme.

Under the assumption of quasi-steady state, we can use Michaelis-Menten kinetics (cf. Equation (2.20)) to deduce that

$$c^{(\mathrm{prod})} = c_{\mathrm{e}} \frac{c^{(\mathrm{sub})}}{K + c^{(\mathrm{sub})}}$$

with $K := \frac{k_-}{k_+}$, which upon substitution into Equation (2.24) yields

$$J = \left(\frac{D_{\mathrm{s}}}{L} + \frac{D_{\mathrm{e}}}{L} \frac{c_{\mathrm{e}} K}{(K + c^{(\mathrm{sub})}\big|_{x=0})(K + c^{(\mathrm{sub})}\big|_{x=L})} \right) \left(c^{(\mathrm{sub})}\big|_{x=0} - c^{(\mathrm{sub})}\big|_{x=L} \right). \tag{2.25}$$

For the sake of notational simplicity, we will rewrite Equation (2.25) into the form

$$J = \left(\kappa_{\mathrm{f}}^{(1)} + \frac{\kappa_{\mathrm{f}}^{(2)}}{(K_{\mathrm{f}} + c^{(\mathrm{sub})}\big|_{x=0})(K_{\mathrm{f}} + c^{(\mathrm{sub})}\big|_{x=L})} \right) \left(c^{(\mathrm{sub})}\big|_{x=0} - c^{(\mathrm{sub})}\big|_{x=L} \right), \quad (2.26)$$

where we have defined

$$\kappa_{\mathrm{f}}^{(1)} := \frac{D_{\mathrm{s}}}{L}, \quad \kappa_{\mathrm{f}}^{(2)} := \frac{D_{\mathrm{e}} c_{\mathrm{e}} K}{L}, \quad K_{\mathrm{f}} := K.$$

Summary of Assumptions

In deriving the final formulae for exchange fluxes (2.20) and (2.26), several assumptions on the reaction and species properties were made. We will summarize them here for the sake of clarity.

For the active enzymatic transport we assumed that

- the complex forms and breaks down at essentially equal rates, leading to the quasi-steady-state approximation,

- the enzyme concentration is significantly lower than the substrate concentration.

For transport by facilitated diffusion we assumed

- that the diffusivities of the product and the enzyme are essentially equal,

- quasi-steady state for the enzymatic reaction,

- that the enzymatic reaction was taking place in a 1D continuum.

If the resulting model presented below is to be applied to a real-world system, then it is crucial to verify that these assumptions are indeed valid. However, as Keener et al. [2009] remarks, the above formulae are used beyond the scope of their theoretical validity quite frequently, and give satisfying results even in scenarios where one or more assumptions are violated.
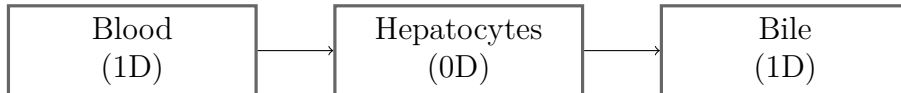
2.4   Compartment Model

In the previous sections, we have described methods for modelling the behavior of individual parts of the blood – hepatocytes – bile system, as well as interactions between them. This means that we are now sufficiently equipped to formulate the governing equations for compound transport across the whole system.

For the sake of simplicity, we assume that it is sufficient to model a single blood capillary going straight from the portal vein to the central vein communicating with a single row of (non-interacting) hepatocytes, which in turn communicate with a single blood canaliculus going all the way from the central vein area towards the portal vein area, parallel to the row of hepatocytes and the blood capillary. This setup is hardly realistic in view of the complexity of vascular and biliary networks inside liver lobules, but nevertheless serves as a good prototype for liver lobule function, at least qualitatively. To make the model closer to reality, we could interpret modelled quantities as *effective* counterparts of the real-world fields. This would amount to interpreting, e.g., the blood capillary in the model as a representation of a group or a network of multiple smaller capillaries. Exact quantification of the effective parameters with respect to their real-world counterparts requires detailed analysis of capillary and canalicular network properties, and is beyond the scope of this work. However, it is a promising project for future work. In Chapter 4, we explore possible extensions of this model further.

In view of the above assumptions about the system, it is natural to view it as a *compartment model*. Usually, compartment models consist of several

isolated entities called *compartments* that interact with each other, and from a mathematical point of view take the form of a system of ODEs. Indeed, transport in the blood – hepatocyte – bile system has been modelled in this way before by Audebert and Vignon-Clementel [2018]. In our model, however, the eventual goal is to capture spatial variations of compound transport mechanisms along the PV-CV axis. An ODE-only model would therefore be insufficient.

The key idea in devising the model is to extend the equations in the blood and bile compartments to include flow and diffusion, coupling them with the ODE-driven hepatocyte compartment. As a result, we get a *1D-0D-1D model* described schematically in Figure 2.3.

| Blood (1D) | → | Hepatocytes (0D) | → | Bile (1D) |

Figure 2.3: Schematic representation of the 1D-0D-1D compartment model.

With this general scheme in mind, we now proceed to formulating governing equations in individual compartments using the mixture theory formulation from Section 2.1.2 and the model reduction strategy from Section 2.2. Note that in this case we can treat flow and transport separately, since the equations for transport take computed velocity fields as input. Although the main point of interest of this thesis is to model transport, we will start by a brief illustration of a possible strategy for modelling flow in the blood and the bile compartments under the assumption that the two flows are coupled.

Before we start, we summarize the notation used in what follows.

- In notating the modelled quantities, the individual compartments are distinguished by superscripts: (S) for blood[3], (H) for hepatocytes, and (B) for bile.

- We use capital letters to denote cross-section-averaged quantities, namely

$$\overline{c_\alpha} =: C_\alpha, \quad \overline{v_z} =: U.$$

- Individual mixture components in the blood and the bile compartments will be distinguished by an index α. For the sake of generality, we assume the tracer fluid to be an N-component mixture, which implies that we are modelling $N+1$-component mixtures in both 1D compartments, the $N+1$-th component being either blood plasma or bile. However, thanks to the mass additivity assumption (2.2), we only need to prescribe governing equations for the N tracer mixture components, as the remaining concentrations are given by

$$C_{N+1}^{(S)} = 1 - \sum_{\alpha=1}^{N} C_\alpha^{(S)}, \quad C_{N+1}^{(B)} = 1 - \sum_{\alpha=1}^{N} C_\alpha^{(B)}.$$

2.4.1 Flow in Blood and Bile: Double Perfusion

From a physiological point of view, it is natural to assume that the fluid mixtures in blood and bile are not independent, even beyond sharing the common components

---

[3]This inspired by the French "sang".

transported from blood to bile via hepatocytes. To model this, we can take the concept of *double perfusion* used, e.g., by Kociánová [2019] and Rohan et al. [2021b] to model the coupling of arterial and venous networks in liver micro-architecture. To illustrate this approach, we present it in a simplified 1D setting, where it can be solved analytically.

The governing equations for stationary two-compartment porous medium flow under the action of no external forces follow from *Darcy's law*, and read

$$
\begin{cases}
-\dfrac{\partial}{\partial z}\left(H^{(\mathrm{S})}\dfrac{\partial p^{(\mathrm{S})}}{\partial z}\right) + G\left(p^{(\mathrm{S})} - p^{(\mathrm{B})}\right) = 0, \\[2mm]
-\dfrac{\partial}{\partial z}\left(H^{(\mathrm{B})}\dfrac{\partial p^{(\mathrm{B})}}{\partial z}\right) + G\left(p^{(\mathrm{B})} - p^{(\mathrm{S})}\right) = 0,
\end{cases}
\tag{2.27}
$$

In the above equations, $H^{(\mathrm{S})}$ and $H^{(\mathrm{B})}$ denote the permeabilities in blood and bile respectively, $p^{(\mathrm{S})}$ and $p^{(\mathrm{B})}$ denote the respective pressures, and finally G is the permeability of the two compartments. The velocities in blood and bile are then given by Darcy's law as

$$
v_z^{(\mathrm{S,B})} = -H^{(\mathrm{S,B})}\frac{\partial p^{(\mathrm{S,B})}}{\partial z}.
$$

Analytic resolution of the system (2.27) with different types of boundary conditions is presented in detail in Appendix A. For the purposes of the compartment model presented here, we prescribe pressure values at both ends of the PV-CV axis in blood. In bile, we prescribe a pressure at the portal vein and assume zero velocity at the central vein. Together, these boundary conditions read

$$
p^{(\mathrm{S})}\big|_{z=0} = P_{\mathrm{PV}}^{(\mathrm{S})}, \quad p^{(\mathrm{S})}\big|_{z=L} = P_{\mathrm{CV}}^{(\mathrm{S})}, \quad p^{(\mathrm{B})}\big|_{z=0} = P_{\mathrm{PV}}^{(\mathrm{B})}, \quad v_z^{(\mathrm{B})}\big|_{z=L} = 0,
$$

with $z = 0$ being the PV end, and $z = L$ the CV end. We will discuss this particular choice of boundary conditions in Chapter 4.

Having illustrated a possible approach to modelling flow in the blood – hepatocytes – bile system, we now continue by presenting governing equations for fluorescent tracer transport.

2.4.2 Blood Compartment

In 3D, we model the blood compartment as an axisymmetric deformable tube of variable radius $R^{(\mathrm{S})}(t,z)$ and length L. In 1D, only the length dimension constitutes the computational domain. The radius is accounted for in the 1D equations containing vessel cross-section area $A^{(\mathrm{S})}$. The governing equations for the transport of the tracer mixture read

$$
\frac{\partial}{\partial t}\left(A^{(\mathrm{S})}C_\alpha^{(\mathrm{S})}\right) + \frac{\partial}{\partial z}\left(\omega_\alpha^{(\mathrm{S})}A^{(\mathrm{S})}U^{(\mathrm{S})}C_\alpha^{(\mathrm{S})}\right) - k_\alpha^{(\mathrm{S})}\frac{\partial^2}{\partial z^2}\left(A^{(\mathrm{S})}C_\alpha^{(\mathrm{S})}\right)
$$
$$
= \left(\kappa_{\mathrm{f}}^{(1)} + \frac{\kappa_{\mathrm{f}}^{(2)}}{(K_{\mathrm{f}} + A^{(\mathrm{H})}C_{\alpha,1}^{(\mathrm{H})})(K_{\mathrm{f}} + A^{(\mathrm{S})}C_\alpha^{(\mathrm{S})})}\right)\left(A^{(\mathrm{H})}C_{\alpha,1}^{(\mathrm{H})} - A^{(\mathrm{S})}C_\alpha^{(\mathrm{S})}\right), \tag{2.28}
$$
$$
\alpha = 1, \ldots, N,
$$

where $k_\alpha^{(\mathrm{S})}$ is the scalar diffusion coefficient for the α-th component of the mixture, and the rest of the symbols follows the notation outlined above. The right-hand side represents the concentration flux at the vessel boundary, namely the uptake of compounds from blood to hepatocytes by facilitated diffusion.

2.4.3 Hepatocyte Compartment

Once the tracer mixture enters the hepatocytes, its components possibly undergo multiple chemical reactions before the final products are secreted into bile. To account for this, we assume that the α-th component undergoes $M_\alpha - 1$ reactions

$$\alpha_1 \to \alpha_2 \to \cdots \to \alpha_{M_\alpha},$$
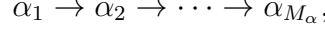
with α_1 being the compound entering the hepatocytes and α_{M_α} the final product secreted into bile. We denote by $C_{\alpha,i}^{(H)}$ the concentration of the intermediate compound α_i and, if convenient, we use the vector notation $\boldsymbol{C}_\alpha^{(H)} := (C_{\alpha,1}^{(H)}, \ldots, C_{\alpha,M_\alpha}^{(H)})^T$ for all the compounds entering into the α-th compound chain. Using this vector notation, we can write the ODE for reaction rates collectively as

$$\frac{\mathrm{d}\boldsymbol{C}_\alpha^{(H)}}{\mathrm{d}t} = \boldsymbol{f}_\alpha, \quad \alpha = 1, \ldots, N,$$

where $\boldsymbol{f}_\alpha := (f_{\alpha,1}, \ldots, f_{\alpha,M_\alpha})$ is the vector of reaction rates.

We couple the 0D model described above by viewing the time derivative in the ODE as a partial derivative, and by adding terms characterizing uptake of tracer mixture by facilitated diffusion from blood and active secretion of the products into bile. The final system of equations reads

$$
\begin{aligned}
\frac{\partial}{\partial t}\left(A^{(H)}C_{\alpha,i}^{(H)}\right) &= \left(\kappa_f^{(1)} + \frac{\kappa_f^{(2)}}{(K_f + A^{(S)}C^{(S)})(K_f + A^{(H)}C_{\alpha,i}^{(H)})}\right) \\
&\times \left(A^{(S)}C_\alpha^{(S)} - A^{(H)}C_{\alpha,i}^{(H)}\right) - \frac{V_{\max}A^{(H)}C_{\alpha,i}^{(H)}}{K_m + A^{(H)}C_{\alpha,i}^{(H)}} + f_{\alpha,i}(A^{(H)}\boldsymbol{C}_\alpha^{(H)}), \\
&\qquad\qquad i = 1, \ldots, M_\alpha, \ \alpha = 1, \ldots, N,
\end{aligned}
\tag{2.29}
$$

2.4.4 Bile Compartment

The model for the bile compartment is analogous in structure to the blood compartment, although the difference in parameter values and consequently also in dominant transport mechanisms is notable (cf. discussion in Section 2.1.1). The governing equations in this compartment read

$$
\begin{aligned}
\frac{\partial}{\partial t}\left(A^{(B)}C_\alpha^{(B)}\right) &+ \frac{\partial}{\partial z}\left(\omega_\alpha^{(B)}A^{(B)}U^{(B)}C_\alpha^{(B)}\right) - k^{(B)}\frac{\partial^2}{\partial z^2}\left(A^{(B)}C_\alpha^{(B)}\right) \\
&= \frac{V_{\max}A^{(H)}C_{\alpha,M_\alpha}^{(H)}}{K_m + A^{(H)}C_{\alpha,M_\alpha}^{(H)}}, \quad \alpha = 1, \ldots, N,
\end{aligned}
\tag{2.30}
$$

Chapter Summary This chapter was devoted to the derivation of a prototype 1D-0D-1D compartment model of the blood – hepatocytes – bile system inside the liver lobule. We started by formulating 3D governing equations for flow and transport inside the 1D compartments using the framework of mixture theory. We then presented a model reduction strategy that we compared to strategies in reference literature giving different results, pointing out the differences and the

pitfalls of reference derivations. We then proposed a modification of the approach from literature that would lead to the same results as our approach. After briefly presenting models of compound transport via active enzymatic secretion and facilitated diffusion, we finished by formulating the governing equations for fluorescent marker transport in the blood – hepatocytes – bile system, and discussing a simple model of flow by double perfusion.

Chapter 3

Numerical Experiments

In the following chapter, we present illustrative numerical simulations for the model presented in Chapter 2. Since that model is still relatively general, we consider a few particular, simple but representative, scenarios that are appropriate for the physiological system in question. Extending these into a more general form should be straightforward, presenting much more a technical difficulty than a conceptual one.

We will start by recalling the governing equations for the compartment model along with simplifying assumptions made in the numerical experiments. We will then describe in detail the numerical implementation of those equations and discuss possible modifications and improvements. To conclude the chapter, we will list and comment on the values of parameters used, and present the results of the numerical experiments.

3.1   Governing Equations

To start with, suppose in what follows that the tracer fluid only has *one component* that *does not participate in any reactions* inside the hepatocytes, implying that $N = 1$, $M_1 = 1$ in Equations (2.28) – (2.30), and we can omit corresponding subscripts in the notation. Furthermore, absence of reactions in hepatocytes means that $\boldsymbol{f}_\alpha \equiv \boldsymbol{0}$ in Equation (2.29). Although drastic at first sight, this simplification actually describes the real transport properties of several fluorescent tracers used in practice (cf. de Waart et al. [2010] or Mills et al. [1997] among others).

The flow in 1D compartments follows from the double perfusion model described in Section 2.4.1, and the system of corresponding governing equations (2.27) can be solved analytically. For clarity, we recall the considered boundary conditions

$$p^{(\mathrm{S})}\big|_{z=0} = P_{\mathrm{PV}}^{(\mathrm{S})}, \quad p^{(\mathrm{S})}\big|_{z=L} = P_{\mathrm{CV}}^{(\mathrm{S})}, \quad p^{(\mathrm{B})}\big|_{z=0} = P_{\mathrm{PV}}^{(\mathrm{B})}, \quad v_z^{(\mathrm{B})}\big|_{z=L} = 0.$$

For the purposes of the numerical experiments in this chapter, we have chosen

$$H^{(\mathrm{S})} = 2, \quad H^{(\mathrm{B})} = 5, \quad G = 1, \quad P_{\mathrm{PV}}^{(\mathrm{S})} = 4, \quad P_{\mathrm{CV}}^{(\mathrm{S})} = 1, \quad P_{\mathrm{PV}}^{(\mathrm{B})} = -2$$

as parameter values. Their role is purely illustrative. Real-world parameters will be discussed in Chapter 4. The velocity profiles in blood and bile thus obtained are shown in Figure 3.1.

Under the above assumptions, the governing equations for the 1D-0D-1D transport model, along with the initial and boundary conditions, read

$$\frac{\partial}{\partial t}\left(A^{(\mathrm{S})}C^{(\mathrm{S})}\right) + \frac{\partial}{\partial z}\left(\omega^{(\mathrm{S})}A^{(\mathrm{S})}U^{(\mathrm{S})}C^{(\mathrm{S})}\right) - k^{(\mathrm{S})}\frac{\partial^2}{\partial z^2}\left(A^{(\mathrm{S})}C^{(\mathrm{S})}\right)$$
$$= \left(\kappa_{\mathrm{f}}^{(1)} + \frac{\kappa_{\mathrm{f}}^{(2)}}{(K_{\mathrm{f}} + A^{(\mathrm{H})}C^{(\mathrm{H})})(K_{\mathrm{f}} + A^{(\mathrm{S})}C^{(\mathrm{S})})}\right)\left(A^{(\mathrm{H})}C^{(\mathrm{H})} - A^{(\mathrm{S})}C^{(\mathrm{S})}\right), \tag{3.1}$$

$$\frac{\partial}{\partial t}\left(A^{(\mathrm{H})}C^{(\mathrm{H})}\right) = \left(\kappa_{\mathrm{f}}^{(1)} + \frac{\kappa_{\mathrm{f}}^{(2)}}{(K_{\mathrm{f}} + A^{(\mathrm{H})}C^{(\mathrm{H})})(K_{\mathrm{f}} + A^{(\mathrm{S})}C^{(\mathrm{S})})}\right)$$
$$\times \left(A^{(\mathrm{S})}C^{(\mathrm{S})} - A^{(\mathrm{H})}C^{(\mathrm{H})}\right) - \frac{V_{\max}A^{(\mathrm{H})}C^{(\mathrm{H})}}{K_{\mathrm{m}} + A^{(\mathrm{H})}C^{(\mathrm{H})}}, \tag{3.2}$$

$$\frac{\partial}{\partial t}\left(A^{(\mathrm{B})}C^{(\mathrm{B})}\right) + \frac{\partial}{\partial z}\left(\omega^{(\mathrm{B})}A^{(\mathrm{B})}U^{(\mathrm{B})}C^{(\mathrm{B})}\right) - k^{(\mathrm{B})}\frac{\partial^2}{\partial z^2}\left(A^{(\mathrm{B})}C^{(\mathrm{B})}\right)$$
$$= \frac{V_{\max}A^{(\mathrm{H})}C^{(\mathrm{H})}}{K_{\mathrm{m}} + A^{(\mathrm{H})}C^{(\mathrm{H})}}, \tag{3.3}$$

$$C^{(\mathrm{S})}\Big|_{t=0} = C^{(\mathrm{H})}\Big|_{t=0} = C^{(\mathrm{B})}\Big|_{t=0} = 0, \tag{3.4}$$

$$C^{(\mathrm{S})}\Big|_{z=0} = g(t), \quad k^{(\mathrm{S})}\frac{\partial}{\partial z}\left(A^{(\mathrm{S})}C^{(\mathrm{S})}\right)\Big|_{z=L} = 0, \tag{3.5}$$

$$k^{(\mathrm{B})}\frac{\partial}{\partial z}\left(A^{(\mathrm{B})}C^{(\mathrm{B})}\right)\Big|_{z=L} = 0, \quad C^{(\mathrm{B})}\Big|_{z=L} = 0. \tag{3.6}$$

While the arguments behind prescribing the governing equations in this specific form have been discussed at length in Chapter 2, we still need to justify, or at least motivate, the choice of initial and boundary conditions.

As initial conditions, we prescribe zero concentration in all compartments at $t = 0$ in Equation (3.4). This is the natural choice given the real-world context of the model.

The inlet ($z = 0$) boundary condition in the blood compartment is given by a prescribed input concentration profile, representing the time evolution of the concentration of the injected tracer. The concentration profiles that are usually prescribed are presented below.

1. The *square impulse* translates to a uniform concentration profile in a chosen time window and is expressed mathematically as

$$g_\alpha(t) = c_0\chi_{[t_0,t_1]}(t), \quad c_0 > 0, \, t_0, t_1 \in [0, T].$$

2. The *Gaussian impulse* has the familiar form

$$g_\alpha(t) = c_0\frac{1}{\sigma\sqrt{2\pi}}\exp\left[-\frac{(t - \alpha t_0)^2}{(2\sigma^2)}\right], \quad c_0, \sigma, \alpha > 0, \, t_0 \in [0, T].$$

3. The *arterial input function (AIF)* approximates the arterial pulse and, according to Parker et al. [2006], has the form

$$g_\alpha(t) = c_1(t) + c_2(t) + \alpha \frac{\exp{(-\beta t)}}{1 + \exp{[-s(t - \tau)]}},$$

$$c_i(t) = \frac{A_i}{\sigma_i \sqrt{2\pi}} \exp{\left[-\frac{(t - T_i)^2}{(2\sigma_i)^2} \right]}, \quad i = 1, 2,$$

$$A_1, A_2, \sigma_1, \sigma_2, \alpha, \beta, s > 0, \ T_1, T_2, \tau \in [0, T].$$

4. The most realistic option is to use *interpolated experimental data.*

Illustrative plots of the above input concentration profiles are in Figure 3.2. Even though the choice of parameters was a mere matter of convenience, we list the parameter values here for reference:

- step/square impulse: $c_0 = 1$, $t_0 = 0.05$, $t_1 = 0.25$,

- Gaussian impulse: $c_0 = 0.125$, $\sigma = 0.05$, $\alpha = 1$, $t_0 = 0.15$,

- AIF: $A_1 = A_2 = 0.0375$, $\sigma_1 = 0.18$, $\sigma_2 = 7$, $\alpha = 2.705$, $\beta = 4.62$, $s = 47.56$, $T_1 = 0.188$, $T_2 = 0.496$, $\tau = 0.23$.

At the outlet $(z = L)$, we decided to impose zero diffusive flux. The interpretation of this condition is that we assume that, at the outflow boundary, the tracer is simply advected with blood into the central vein.

The boundary conditions in the bile compartment are analogous to the blood compartment, with zero concentration prescribed at the inlet $(z = L$, which is opposite to blood because of the different directions of blood and bile flow) meaning that there is no tracer injected directly into the bile canaliculi.
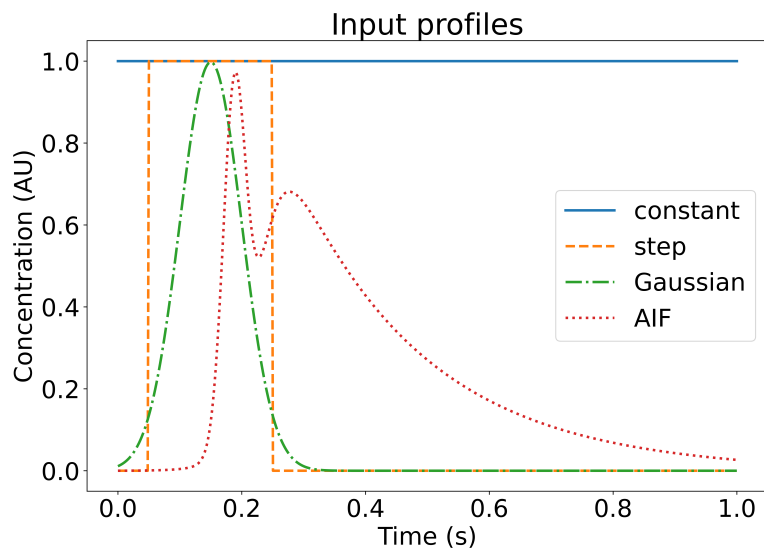
3.2 Numerical Implementation

The numerical schemes used to find approximate solutions of the system (3.3) – (3.6) were chosen to be very simple, mainly for implementation convenience reasons. This has obvious drawbacks in terms of the implementation stability and efficiency that we will address in more detail in Chapter 4. Nevertheless, the chosen numerical methods lead to promising proof-of-concept results presented below.

More specifically, the IBVPs in blood and bile are essentially hyperbolic equations, which is one of the motivations for using the *finite volume method* to solve both, another motivation being that parts of the implementation used in this thesis were adapted from Boissier et al. [2021]. To approximate the flux in the equations, we used a combination of a simple *upwind flux* with a *central difference* approximation of the diffusion term. The boundary conditions were enforced using *ghost cells* (cf. Boissier et al. [2021], LeVeque [2002]). The equation in the hepatocyte compartment is essentially an ODE, and was solved via the *Runge-Kutta* method of the fourth order. Time-stepping in all numerical schemes was explicit. These numerical schemes were implemented in Python, without using any third-party solver libraries, apart from NumPy for vector manipulation.
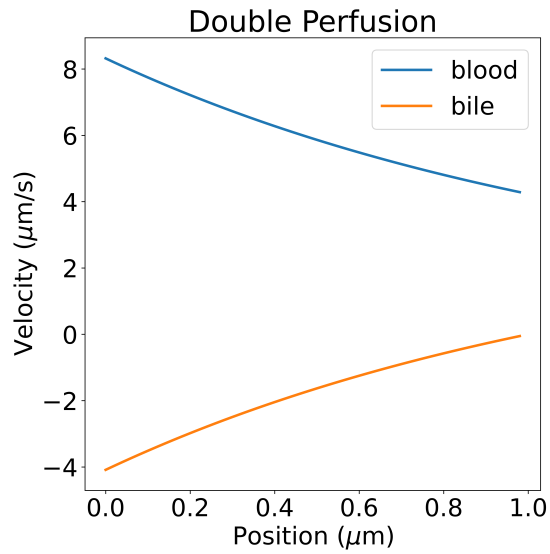
Figure 3.1: Velocity profiles in blood and bile given by the double perfusion model. On the position axis, $0\,\mu m$ would correspond to the PV end of the axis, while $1\,\mu m$ would correspond to the CV end of the axis. Due to an *a priori* arbitrary choice of parameter values, these are purely illustrative, but their relation to real-world values will be discussed in Chapter 4.

Figure 3.2: Different input concentration profiles.

We chose this rather low-level approach due to long-term aims of the numerical implementation discussed in Chapter 4. To test the implementation, numerical solutions obtained with it were compared to analytical results in special scenarios, as we show in Appendix B.

Since the problems in the three compartments are coupled, the same has to be true for the individual solvers. In particular, the right-hand side of the equation in each compartment depends on the concentration in the compartment, as well as the concentration in the neighboring compartment. Thus, at each time step, the solver takes two inputs – the concentration in the compartment at the previous time step, and the most up-to-date concentration in the neighboring compartment, as described in Algorithm 1. A straightforward physical interpretation of this algorithm is that the sequence of solver steps corresponds to the compound passing progressively from blood through hepatocytes into bile. In the algorithm, `FVMStep` denotes the method that runs one step of the finite volume solver, and `RungeKuttaStep` the method that runs one step of the ODE solver.

Algorithm 1 Numerical solution of the system (3.3) – (3.6).

INPUT: blood inlet concentration profile $g(t)$

$\quad C^{(S)}\big|_{t=t_0} := 0, \; C^{(H)}\big|_{t=t_0} := 0, \; C^{(B)}\big|_{t=t_0} := 0$

$\quad$**for** $n = 1, \ldots, N$ **do**

$\qquad C^{(S)}\big|_{t=t_n} \leftarrow \texttt{FVMStep}\left(C^{(S)}\big|_{t=t_{n-1}}, \, C^{(H)}\big|_{t=t_{n-1}} \right)$

$\qquad C^{(H)}\big|_{t=t_n} \leftarrow \texttt{RungeKuttaStep}\left(C^{(H)}\big|_{t=t_{n-1}}, \, C^{(S)}\big|_{t=t_n} \right)$

$\qquad C^{(B)}\big|_{t=t_n} \leftarrow \texttt{FVMStep}\left(C^{(B)}\big|_{t=t_{n-1}}, \, C^{(H)}\big|_{t=t_n} \right)$

$\quad$**end for**

OUTPUT: $\left\{ C^{(S)}\big|_{t=t_n} \right\}_{n=1}^{N}, \; \left\{ C^{(H)}\big|_{t=t_n} \right\}_{n=1}^{N}, \; \left\{ C^{(B)}\big|_{t=t_n} \right\}_{n=1}^{N}$

3.3 Results

In this section, we present results of the numerical simulations for various examples of parameter setup and discuss the observed behavior of the compartment model.

We chose to model two slightly different scenarios, to which we refer as *Scenario 1* and *Scenario 2* in what follows. In Scenario 1, we set the facilitated diffusion parameters to $\kappa_f^{(1)} = 1\,\text{s}^{-1}$, $\kappa_f^{(2)} = 1\,\text{AU}\mu\text{m}^2/\text{s}$, $K_f = 0.05\,\text{AU}\mu\text{m}^2$ and the active secretion parameters to $K_m = 0.5\,\text{AU}\mu\text{m}^2$, $V_{max} = 1\,\text{AU}\mu\text{m}^2/\text{s}$, whereas in Scenario 1, we set the facilitated diffusion parameters to $\kappa_f^{(1)} = 1 \times 10^{-4}\,\text{s}^{-1}$, $\kappa_f^{(2)} = 5 \times 10^{-3}\,\text{AU}\mu\text{m}^2/\text{s}$, $K_f = 0.05\,\text{AU}\mu\text{m}^2$ and the active secretion parameters to $K_m = 0.02\,\text{AU}\mu\text{m}^2$, $V_{max} = 2.5\,\text{AU}\mu\text{m}^2/\text{s}$. The common parameters for both scenarios are listed in Table 3.1.

For Scenario 1, a step input function was used. For Scenario 2, we ran three simulations 2a, 2b, 2c for the step input function, the Gaussian input function, and AIF respectively. The time-space plots of solutions for all four simulations are shown in Figures 3.3 – 3.6. Although the parameters used in the scenarios

Table 3.1: Simulation parameter values common to Scenario 1 and Scenario 2.

Quantity	Symbol	Value
General		
Time step (s)	Δt	5×10^{-5}
Initial time (s)	t_0	0
Final time (s)	T	1
Space step (µm)	Δz	0.02
Lobule radius (µm)	L	1
Blood compartment		
Vessel radius (µm)	$R^{(\mathrm{S})}$	1
Correlation coefficient	$\omega^{(\mathrm{S})}$	1
Diffusivity ($\mathrm{µm^2\,s^{-1}}$)	$k^{(\mathrm{S})}$	3
Bile compartment		
Vessel radius (µm)	$R^{(\mathrm{S})}$	1
Correlation coefficient	$\omega^{(\mathrm{S})}$	1
Diffusivity ($\mathrm{µm^2\,s^{-1}}$)	$k^{(\mathrm{S})}$	3

serve merely to illustrate the model output, we can still try to provide possible physiological interpretations of the solution behavior.
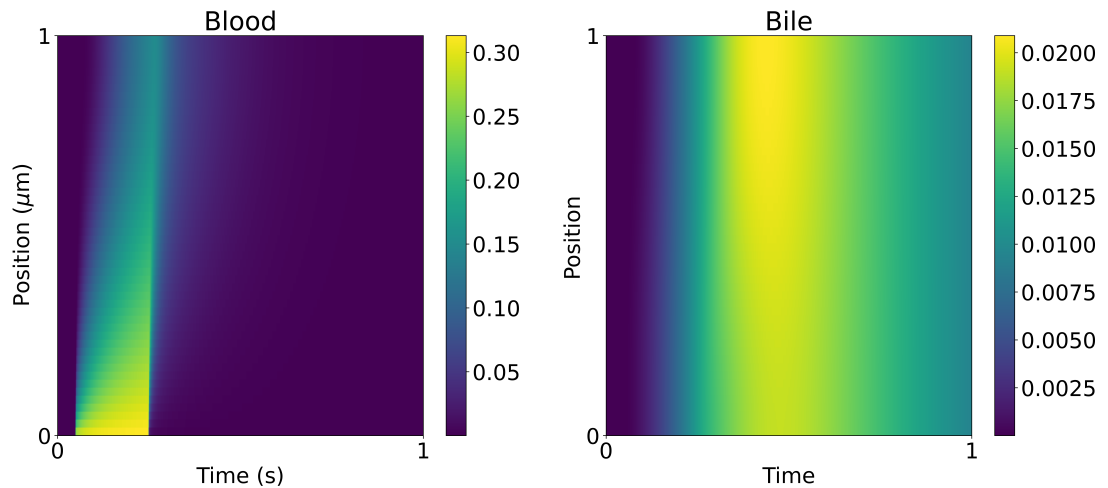
Scenario 1 is represented in Figure 3.3. Here, the uptake and secretion in hepatocytes are the dominant mechanisms. Indeed, as soon as the compound is injected into blood and starts diffusing along the PV-CV axis, non-zero concentrations in bile appear almost immediately. The concentration in bile is relatively uniform in space, which suggests that the uptake and secretion mechanisms are saturated everywhere. This motivates the choice of lower values for exchange parameters to investigate behavior in cases where uptake and secretion are not necessarily dominant.

From Figure 3.4, we clearly see that the uptake and secretion are indeed no longer dominant in Scenario 2a. This is manifested by a slower decrease in concentration along the PV-CV axis in blood, as well as the slower rise in concentrations in bile. After some time, the exchange mechanisms get saturated, but only in the pericentral region. Similarly to Scenario 2a, non-trivial concentration in bile appears in two "waves" in Scenario 2b (cf. Figure 3.5). However, the first "wave" is considerably larger than in Scenario 2a. In Figure 3.6, representing Scenario 2c, we only see one "wave" of non-trivial concentration in bile, which is in contrast with Scenarios 2a and 2b. This "wave" is then followed by a progressive saturation of the uptake and secretion mechanisms caused by the longer tail of the AIF. This saturation is relatively uniform, but is slower than in Scenario 1 due to lower uptake and secretion rates.

We can also see that while concentrations in bile are lower by approximately an order of magnitude compared to concentrations in blood in Scenario one, this difference is of up to four orders of magnitude in Scenario 2. This is due to the lower values of exchange rates, meaning, that less of the compound actually gets across the blood – hepatocytes and hepatocytes – bile interfaces.

As a final remark, we recall and emphasize that the purpose of the numerical experiments presented above was to illustrate different behaviors of the compartment model. The results presented here have little pertinence to a real-world human or animal liver lobule. Nevertheless, the interpretation of the results for a more realistic setup would be analogous, the core being the identification of the dominant transport mechanisms and their impact on the solution behavior.

Chapter Summary   This chapter illustrated the behavior of the previously presented compartment model by several numerical experiments. These have shown that, based on the choice of parameter values in the model, different transport mechanisms among advection, diffusion, active secretion, and facilitated diffusion can be interpreted as dominant. This aspect of the solution behavior can be used in the future to calibrate the model parameters to fit a real-world experimental setup.
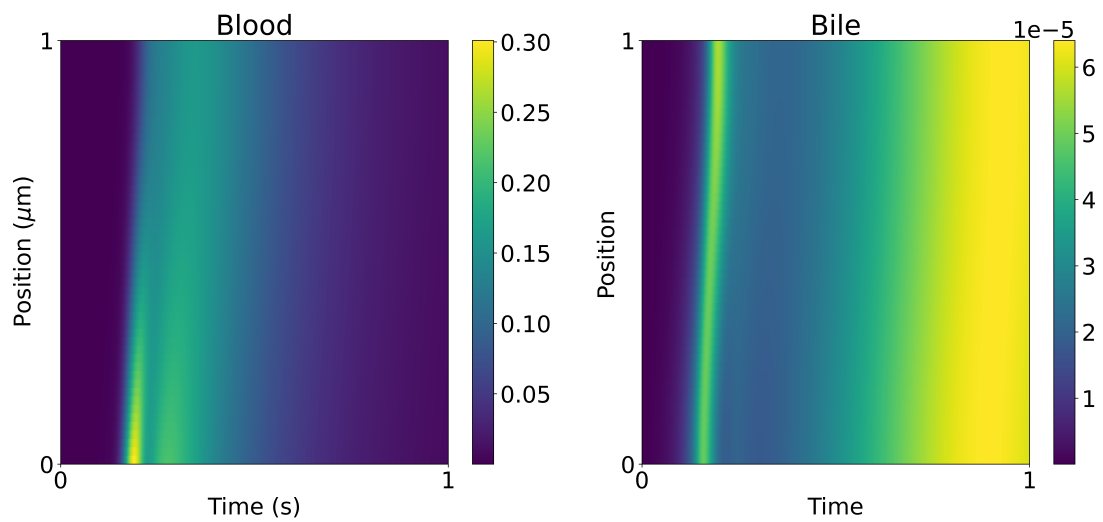

Figure 3.3: Time-space solution plot for Scenario 1. We can see that, in this scenario, the uptake and secretion in hepatocytes are the dominant mechanisms. Once the compound is injected into blood and starts diffusing along the PV-CV axis, non-zero concentrations in bile appear almost immediately. The concentration in bile is relatively uniform in space, which suggests that the uptake and secretion mechanisms are saturated everywhere.
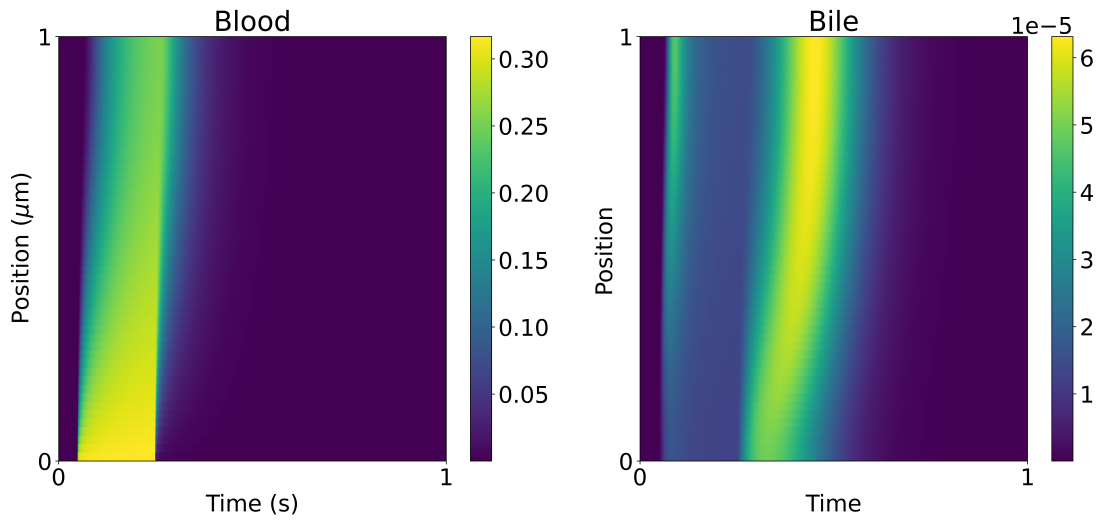
Figure 3.4: Time-space solution plot for Scenario 2a. Compared to Scenario 1 (cf. Figure 3.3), the uptake and secretion are no longer dominant, which is apparent from the slower decrease in concentration along the PV-CV axis in blood, as well as the slower rise in concentrations in bile. After some time, they get saturated, but only in the pericentral region.
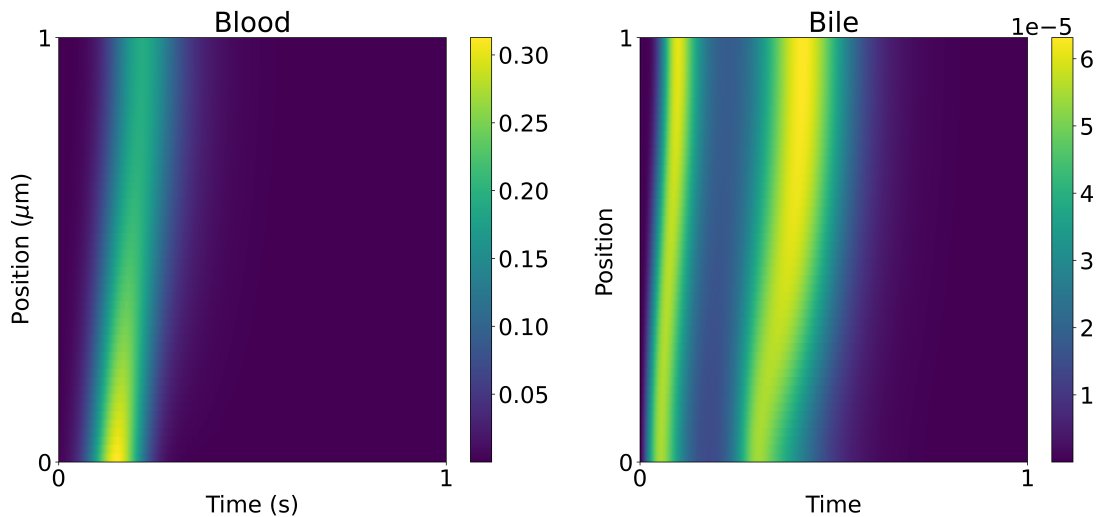
Figure 3.5: Time-space solution plot for Scenario 2b. Similarly to Scenario 2a (cf. Figure 3.4), non-trivial concentration in bile appears in two "waves". However, the first "wave" is considerably larger than in Scenario 2a.

Figure 3.6: Time-space solution plot for Scenario 2c. Contrary to Scenarios 2a (cf. Figure 3.4) and 2b (cf. Figure 3.5), we only see one "wave" of non-trivial concentration in bile. This "wave" is then followed by a progressive saturation of the uptake and secretion mechanisms caused by the longer tail of the AIF. This saturation is relatively uniform, but is slower than in Scenario 1 due to lower uptake and secretion rates.

Chapter 4

Discussion and Outline of Future Work

4.1 Modelling Assumptions

The liver lobule, like virtually all physiological systems, is an extremely complex system. In modelling its behavior, numerous assumptions had to be made, and the choice of these assumptions is in no way unique.

4.1.1 Model Geometry

First, the compartment model proposed in this thesis models the PV-CV axis as one straight line, along which there is a blood vessel, a row of hepatocytes, and a bile canaliculus. Considering the complexity of the vascular and biliary networks in the real lobule, this is obviously a crude over-simplification of the actual system geometry. Nevertheless, there are several ways of extending the modelling and numerical results obtained in this simplified setting to more realistic, and thus more complex, geometries.

One consists in localizing the model scope to network branches instead of the entire PV-CV axis. In their simulation of micro-circulation and transport inside liver lobules, Boissier et al. [2021] and Dichamp et al. [2023] solve 1D governing equations (under the assumption of stationary laminar flow of a Newtonian fluid in a cylindrical vessel these yield the well-known Poiseuille flow) in individual vascular network branches and match them at bifurcations according to appropriate rules. Similarly, the compartment model presented in this thesis could be adapted to more complex lobule geometries by restricting the governing equations (3.1), (3.2), and (3.3) to simple segments of the particular geometry and subsequently matching the solutions using appropriate boundary conditions.

This point of view is complicated by the fact that, in a realistic lobule geometry, the blood and bile networks are *a priori* different. While this is an inconvenience in terms of numerical implementation of the model, it is not a conceptual issue. Furthermore, this approach favors separate treatment of the hepatocyte compartment by individual cells. In addition to being more realistic, it therefore leads itself naturally to cooperation with cellular models of liver tissue.

Another way of extending the proposed model is to re-interpret the current model geometry as an *effective* representation of the PV-CV axis across the lobule.

For this approach, rather than considering the detail of vessel networks, we assume that the lobule cross-section is radially symmetric, which is reasonably close to the hexagonal cross-section geometry and more convenient for the presentation of the approach. In this setting, the 1D-0D-1D compartment model can be viewed as a reduced model of the radially symmetric lobule in the radial direction, corresponding to the PV-CV axis. The model parameters would then represent effective values of their real-world counterparts, capturing both the compartment structure and properties averaged over the corresponding circular radius on the axis. The basis for this point of view is already present in the model, in the form of double perfusion governing equations for flow. Instead of exact vascular tree geometries, these equations consider the blood and biliary networks as coupled porous media described by the permeabilities that implicitly carry information about network structure. Although very coarse on the microscopic level, this approach leads naturally to multi-scale models and methods such as homogenization, as used for example by Rohan et al. [2021a].

In deciding which of these two approaches is preferable, available data as well as intended use of results have to be taken into account. Ideally, a correspondence between the approaches should be designed, so that they can coexist and communicate, thus making the extension applicable to a multiscale model, for example of the entire liver.

4.1.2 Dimensional Analysis

The aim of numerical experiments presented in Chapter 3 was mainly to show a proof-of-concept numerical implementation of the compartment model and to illustrate solution behavior in a few particular cases. Hence, values of simulation parameters were chosen with little regard for the real-world lobule, focusing rather on the direct impact of parameter value choice on the behavior of the model. Furthermore, the task of choosing realistic parameter values is not completely straight-forward because, due to the microscopic nature of the modeled system, parameter values are often not available at all, or have relatively wide ranges. For reference, we provide some representative values of key parameters, or their estimates, used in other studies in Table 4.1.[1] Since the long-term goal is to reproduce results of experiments on mice, the values provided are relevant to the mouse liver lobule.[1]

With these concrete parameter values, we can in particular assess the system dimensions and confront them with the model assumptions described in the previous chapters. To do so, we will compute several dimensionless constants characterizing fluid behavior, namely

- the *Knudsen number* Kn defined by

$$\text{Kn} = \frac{\text{Ma}}{\text{Re}}\sqrt{\frac{\gamma\pi}{2}},$$

---

[1]Boissier [2018] in fact uses arbitrary values of diffusion coefficients for numerical simulations in bile. However, the value given in Table 4.1 is presented as a reference for diffusion in blood. We re-use this value for bile, based on assumption of similar properties of the two fluids.

[1]Li et al. in fact models human biliary system. However, we suspect that properties such as density and viscosity should not differ significantly between the bile of mice and men.

Table 4.1: Representative values of model parameters for a realistic liver lobule.

Quantity (unit)	Value	Reference
General		
Lobule radius (µm)	250	Boissier [2018]
Blood compartment		
Vessel radius (µm)	3.61	Boissier [2018]
Density ($\mathrm{kg\,m^{-3}}$)	1054	Ahmadi-Badejani et al. [2020]
Viscosity (mPa s)	1.3	Boissier [2018]
Velocity ($\mathrm{\mu m\,s^{-1}}$)	60	Boissier [2018]
Diffusivity ($\mathrm{\mu m^2\,s^{-1}}$)	150	Boissier [2018]
Bile compartment		
Vessel radius (µm)	0.25	Meyer et al. [2017]
Density ($\mathrm{kg\,m^{-3}}$)	1000	Li et al.
Viscosity (mPa s)	1	Li et al.
Velocity ($\mathrm{\mu m\,s^{-1}}$)	0.785	Meyer et al. [2017]
Diffusivity ($\mathrm{\mu m^2\,s^{-1}}$)	150	Boissier [2018][1]

Ma being the Mach number, Re the Reynolds number (see below), and γ is the ratio of specific heats. The Knudsen number is used to assess whether a given system can be modelled reasonably well by equations of continuum mechanics, or whether a discrete approach using molecular dynamics is necessary (cf. [Laurendeau, 2005, Section 16.2]). The Mach number is defined as the ratio of the characteristic fluid velocity and the speed of the sound in the fluid.

- The *Reynolds number* Re defined by

$$\mathrm{Re} = \frac{\rho v L}{\mu},$$

where ρ is the fluid density, μ is its (dynamic) viscosity, v is the characteristic fluid velocity, and L the characteristic length. The Reynolds number is used to estimate turbulent behavior. Namely, for small Reynolds numbers, the turbulence is virtually non-existent, and we can assume *laminar* flow.

- The *Péclet number* Pe defined by

$$\mathrm{Pe} = \frac{v L}{k},$$

where k is the diffusivity coefficient of the fluid and v, L are as above. The Péclet number is used to characterize the relative dominance of advection and diffusion mechanisms in compound transport problems.

The values of the above-mentioned dimensionless numbers are

- $\mathrm{Kn} \approx 4.85 \times 10^{-6}$, $\mathrm{Re} \approx 0.012$, $\mathrm{Pe} \approx 100$ in blood,

- Kn $\approx 3.94 \times 10^{-6}$, Re $\approx 1.96 \times 10^{-4}$, Pe ≈ 1.3 in bile.

In both cases, Kn $\ll 10$, which means that both blood and bile compartments can be modelled using continuum mechanics. This serves as an *a posteriori* validation of the approach used throughout this thesis. Similarly, Re $\ll 2300$ in both cases, so an assumption of laminar flow in Section 2.4.1 is valid. The values of the Péclet number differ significantly in blood and bile. They suggest that while transport in blood is advection-dominated, it is diffusion dominated in bile. This further supports experimental studies of Vartak et al. [2021b] suggesting that bile salts are transported by diffusion in bile canaliculi.

Additionally, we can compute values of $\varepsilon = R/L$ from Section 2.2.3. Using values from Table 4.1, we get $\varepsilon \approx 0.014$ in blood and $\varepsilon \approx 0.001$ in bile, which means that the modelling assumption $\varepsilon \ll 1$ is valid in both compartments.

4.1.3 Boundary Conditions

In specifying the model setup used in numerical experiments in Chapter 3, we imposed boundary conditions for both double perfusion flow and compound transport. Here, we discuss the choice of boundary conditions briefly and outline alternative possibilities.

First, for the double perfusion, we prescribed pressure values at both ends of the domain in blood, and in bile we prescribed the pressure at the periportal end and imposed a zero velocity at the pericentral end. The reasoning behind this choice is that, in blood, calculating flow from pressure gradients is commonplace in this type of model, usually by using some variation of Poiseuille flow (cf. Boissier et al. [2021]). As for bile, zero velocity at the pericentral end is connected to the hypothesis that bile originates in the lobule and flows in the direction from the central vein towards the portal vein, hence no inflow is expected at the pericentral end. We decided to prescribe a pressure value at the periportal end of the computational domain to emphasize the difference between pressure values in blood and bile that are at the core of the expected flow behavior. A reasonable alternative to this choice would be to prescribe bile velocity at the pericentral end, provided that accurate measurements of periportal bile duct velocities are available.

Second, the choice of boundary conditions for compound transport could follow the choices established in literature, mainly because the models there only consider one of the competing transport mechanisms (advection for Boissier et al. [2021], diffusion for Vartak et al. [2021b]). If only advection is considered, then an inlet boundary condition is sufficient. The input concentration profile in blood and zero concentration input in bile are obvious choices here. On the other hand, Vartak et al. [2021b] consider transport purely by diffusion in bile and impose a homogeneous Neumann (i.e. zero-gradient) condition at both ends of the PV-CV axis. If both advection and diffusion are considered, the homogeneous Neumann condition is different from the zero-gradient condition. The homogeneous Neumann condition can be interpreted as equating the diffusive flux to the advective term, while the zero-gradient condition implies that there is no diffusion at the ends of the domain and the transport is purely advective there. Since it is reasonable to assume that the transport in periportal bile ducts is advection dominated, we chose the zero-gradient boundary condition.

4.2 Choice of Numerical Methods

As outlined in Section 3.2, the finite volume schemes used to solve the equations in the 1D compartments were of first order in both time and space, with an explicit time-stepping, an upwind flux for the diffusion term, and a central difference approximation for the diffusive term. This is indeed a very simple choice and has its drawbacks. The first is relatively low precision, necessitating small space- and time-steps to capture solution details. Other than that, the presence of the diffusive term in combination with the explicit time-stepping makes the scheme only conditionally stable (cf. LeVeque [2002]), which leads to the need for very small time-steps even for a relatively coarse space resolution, as can be seen from Table 3.1.

Higher precision could be obtained using space discretizations of higher order, as done by Boissier et al. [2021]. However, as Boissier et al. [2021] point out, this introduces *numerical diffusion* into the scheme, which is partially visible even in the first-order scheme, as explained in Appendix B. The issue of numerical diffusion can be overcome by using *slope limiters* (cf. LeVeque [2002], Boissier et al. [2021]).The stability issue introduced by the diffusion term is best treated by using semi-implicit or implicit time-stepping. These issues are therefore purely technical, with plenty of existing research, and were not treated as a part of this thesis to keep the focus on methods of modelling biophysical phenomena.

Before moving on, we briefly remark on the fact that the code for the numerical experiments was implemented directly, without using any solver libraries. Other than being an insightful programming exercise, this was motivated by the long-term goal of embedding the solver for this compartment model into a more complex simulation codebase that calls for a more low-level approach.

4.3 Suggestions for Further Research

The work presented in the thesis was carried out in part in cooperation with the SIMBIOTX team at Inria Saclay Ile-de-France. The team specializes in multiscale models in system medicine, one of the chief aims being to develop digital twins of these systems. Since the initial stages of the project, part of which is this thesis, had a long-term goal of creating a model of transport inside liver micro-architecture that would be sufficiently detailed and descriptive, but also efficient to solve and convenient to implement and embed into a larger ensemble of models constituting together the digital twin of the human liver. The proof-of-concept compartment model is an initial step on this long and fairly ambitious journey.

The following steps should include fine-tuning the model parameters in order to make the simulation results replicate observed experimental behavior. As mentioned in the preceding sections, this is not a straight-forward task due to lack of exact parameter values. This step would therefore consist in carrying out sensitivity analysis for parameters where realistic ranges are known, and trying to fit parameters with unknown values with the help of experimental data. Another task would consist in revising the numerical implementation of the model and re-implementing it into the codebase maintained by the SIMBIOTX team.

Finally, if the model is to be a part of a liver digital twin, its outputs should communicate efficiently with models on different scales, from cell models to whole-

body circulation models. This can be achieved in several ways, using ideas such as the effective radial model outlined above and homogenization techniques.

Chapter Summary This chapter presents discussions on several points addressed in previous chapter. First, we commented on the possible extensions of the currently proposed model to a real-world lobule setting, either by modifying and applying it to individual branches of sinusoidal and biliary networks as well as single hepatocytes, or by taking a more multiscale approach, starting with effective interpretation of model parameters going through to more sophisticated methods such as homogenization. We then provided a coarse dimensional analysis of the real-world liver lobule, effectively validating certain modelling assumptions made previously. After a brief discussion of the possible improvements of the numerical implementation of the model presented here, we outlined the long-term goals of research in this particular topic.

Conclusion

The main goal of this thesis was to derive a reduced compartment model of fluorescent marker transport in the blood – hepatocytes – bile system inside the liver lobule. The model should describe the system in sufficient detail to reproduce all relevant real-world phenomena, while remaining computationally feasible.

Below, we briefly summarize the key points, results, and outlook of the thesis.

- After a general outline of the physiological context of flow and transport in liver micro-architecture we have established the liver lobule as the functional unit of interest. Chemical compounds enter the lobule via branches of the portal vein, and flow along sinusoids towards the central vein. Along the way, they are taken up by neighboring hepatocytes, possibly metabolized, and secreted into bile canaliculi. (cf. Section 1.2)

- For the specific case of fluorescent tracers, the uptake by hepatocytes occurs by facilitated diffusion, while secretion into bile is active. (cf. Section 1.3)

- We have formulated governing equations for flow and transport in blood and bile for a multi-component Class I mixture in 3D to represent the full description of the blood and bile compartments. (cf. Section 2.1.2)

- We have derived 1D reduced forms of these equations using an approach different from the one used in Formaggia et al. [2009]. After exposing possible shortcomings of the approach of Formaggia et al. [2009], we have suggested its modification that would lead to reduced equations equivalent to ours. (cf. Section 2.2)

- We have presented models of exchanges between vessels and surrounding cells by active transport and facilitated diffusion, as derived in Keener et al. [2009]. (cf. Section 2.3)

- We have formulated a 1D-0D-1D compartment model for the blood – hepatocytes – bile system in a simplified, proof-of-concept geometry. (cf. Section 2.4)

- The behavior of the compartment model has been illustrated by several numerical experiments, to which we have provided prototypical interpretations extensible to a more realistic setting. (cf. Section 3.3)

- The main goals for future work in this direction include extending the model to a real-world setting and embedding it into larger multiscale models of liver. (cf. Section 4.3)

Out of the topics treated in Chapter 4, most pertain to tailoring the model to realistic scenarios. One of the main subjects of interest of the SIMBIOTX team at Inria Saclay Ile-de-France is the development of multiscale models of biological systems and digital twins with applications in clinical practice. This highlights the current stream of efforts to enhance cooperation among researchers from different fields to develop a multidisciplinary approach to complex issues such as liver carcinoma.

Although these efforts are not necessarily new, they are still far from established methodology frameworks, which makes research in a multidisciplinary environment very dynamic and positively challenging. Apart from reasonable expertise in their specific field (e.g. mathematical modelling of continuous media), a researcher in a multidisciplinary environment needs to be able to communicate with peers from related fields (e.g. medicine, toxicology) in sufficient detail to understand the possibilities of his contribution to their work, and to use results in those fields to make informed decisions about research in his field. Communication across diverse specializations in a multidisciplinary research group is a nontrivial skill, that is however indispensable for such a research group to function efficiently and produce high quality results.

In addition to its research results, this thesis serves the author as an introduction into the above described world of multidisciplinary medical research and applications of mathematical modelling in a biophysical context. It has broadened the author's vision of applied scientific research, and has helped him to gain a lateral skill set beyond mathematical modelling in physics, which is an undeniable asset in the modern world of science.

Bibliography

R. Ahmadi-Badejani, M. Mosharaf-Dehkordi, and H. Ahmadikia. An image-based geometric model for numerical simulation of blood perfusion within the liver lobules. *Computer Methods in Biomechanics and Biomedical Engineering*, 23(13):987–1004, October 2020. ISSN 1025-5842, 1476-8259. doi: 10.1080/10255842.2020.1782389.

Chloe Audebert and Irene E. Vignon-Clementel. Model and methods to assess hepatic function from indocyanine green fluorescence dynamical measurements of liver tissue. *European Journal of Pharmaceutical Sciences*, 115:304–319, March 2018. ISSN 0928-0987. doi: 10.1016/j.ejps.2018.01.008.

Noemie Boissier. *Mathematical Modeling of Blood and Bile Flow in Healthy and Damaged Liver Micro-Architecture*. PhD thesis, Sorbonne Université, 2018.

Noemie Boissier, Dirk Drasdo, and Irene E. Vignon-Clementel. Simulation of a detoxifying organ function: Focus on hemodynamics modeling and convection-reaction numerical simulation in microcirculatory networks. *International Journal for Numerical Methods in Biomedical Engineering*, 37(2):e3422, 2021. ISSN 2040-7947. doi: 10.1002/cnm.3422.

Carlo D'Angelo. *Multiscale Modelling of Metabolism and Transport Phenomena in Living Tissues*. PhD thesis, EPFL, Lausanne, 2007.

Dirk R. de Waart, Stephanie Häusler, Maria L. H. Vlaming, Cindy Kunne, Emanuel Hänggi, Hans-Jurgen Gruss, Ronald P. J. Oude Elferink, and Bruno Stieger. Hepatic Transport Mechanisms of Cholyl-l-Lysyl-Fluorescein. *Journal of Pharmacology and Experimental Therapeutics*, 334(1):78–86, July 2010. ISSN 0022-3565, 1521-0103. doi: 10.1124/jpet.110.166991.

Jules Dichamp, Geraldine Cellière, Ahmed Ghallab, Reham Hassan, Noemie Boissier, Ute Hofmann, Joerg Reinders, Selahaddin Sezgin, Sebastian Zühlke, Jan Hengstler, and Dirk Drasdo. In-vitro to in-vivo acetaminophen hepatotoxicity extrapolation using classical schemes, pharmaco-dynamic models and a multiscale spatial-temporal liver twin. *Frontiers in Bioengineering and Biotechnology*, 2023.

Luca Formaggia, Alfio Quarteroni, and Alessandro Veneziani, editors. *Cardiovascular Mathematics*. Springer Milan, Milano, 2009. ISBN 978-88-470-1151-9 978-88-470-1152-6. doi: 10.1007/978-88-470-1152-6.

Ahmed Ghallab, Géraldine Cellière, Sebastian G. Henkel, Dominik Driesch, Stefan Hoehme, Ute Hofmann, Sebastian Zellmer, Patricio Godoy, Agapios Sachinidis,

Meinolf Blaszkewicz, Raymond Reif, Rosemarie Marchan, Lars Kuepfer, Dieter Häussinger, Dirk Drasdo, Rolf Gebhardt, and Jan G. Hengstler. Model-guided identification of a therapeutic strategy to reduce hyperammonemia in liver diseases. *Journal of Hepatology*, 64(4):860–871, April 2016. ISSN 1600-0641. doi: 10.1016/j.jhep.2015.11.018.

Thomas Greuter and Vijay H. Shah. Hepatic sinusoids in liver injury, inflammation, and fibrosis: New pathophysiological insights. *Journal of Gastroenterology*, 51 (6):511–519, June 2016. ISSN 1435-5922. doi: 10.1007/s00535-016-1190-4.

Erlend Hodneland, Erik Hanson, Ove Sævareid, Geir Nævdal, Arvid Lundervold, Veronika Šoltészová, Antonella Z. Munthe-Kaas, Andreas Deistung, Jürgen R. Reichenbach, and Jan M. Nordbotten. A new framework for assessing subject-specific whole brain circulation and perfusion using MRI-based measurements and a multi-scale continuous flow model. *PLOS Computational Biology*, 15(6): e1007073, June 2019. ISSN 1553-7358. doi: 10.1371/journal.pcbi.1007073.

Kolumban Hutter and Klaus Jöhnk. *Continuum Methods of Physical Modeling.* Springer, Berlin, Heidelberg, 2004. ISBN 978-3-642-05831-8 978-3-662-06402-3. doi: 10.1007/978-3-662-06402-3.

William James. Is Life Worth Living? *The International Journal of Ethics*, 6(1): 1–24, October 1895. ISSN 1526-422X. doi: 10.1086/intejethi.6.1.2375619.

Toshinori Kamisako, Esteban Gabazza, Tomoaki Ishihara, and Yukihiko Adachi. Molecular aspects of organic compound transport across the plasma membrane of hepatocytes. *Journal of Gastroenterology and Hepatology*, 14(5):405–412, 1999. ISSN 1440-1746. doi: 10.1046/j.1440-1746.1999.01886.x.

James Keener, James Sneyd, S.S. Antman, J.E. Marsden, and L. Sirovich, editors. *Mathematical Physiology*, volume 8/1 of *Interdisciplinary Applied Mathematics.* Springer, New York, NY, 2009. ISBN 978-0-387-75846-6 978-0-387-75847-3. doi: 10.1007/978-0-387-75847-3.

Barbora Kociánová. Mathematical modelling of liver perfusion. Master's thesis, Charles University, Prague, September 2019.

Normand M. Laurendeau. *Statistical Thermodynamics: Fundamentals and Applications.* Cambridge University Press, New York, 2005. ISBN 978-0-521-84635-6.

Randall J. LeVeque. *Finite Volume Methods for Hyperbolic Problems.* Cambridge Texts in Applied Mathematics. Cambridge University Press, Cambridge, 2002. ISBN 978-0-521-00924-9. doi: 10.1017/CBO9780511791253.

W G Li, X Y Luo, A G Johnson, N A Hill, N Bird, and S B Chin. One-Dimensional Models of the Human Biliary System.

Kirstin Meyer, Oleksandr Ostrenko, Georgios Bourantas, Hernan Morales-Navarrete, Natalie Porat-Shliom, Fabian Segovia-Miranda, Hidenori Nonaka, Ali Ghaemi, Jean-Marc Verbavatz, Lutz Brusch, Ivo Sbalzarini, Yannis Kalaidzidis, Roberto Weigert, and Marino Zerial. A Predictive 3D Multi-Scale Model of Biliary Fluid Dynamics in the Liver Lobule. *Cell Systems*, 4(3):277–290.e9, March 2017. ISSN 24054712. doi: 10.1016/j.cels.2017.02.008.

C. O. Mills, P. Milkiewicz, V. Saraswat, and E. Elias. Cholyllysyl fluroscein and related lysyl fluorescein conjugated bile acid analogues. *The Yale Journal of Biology and Medicine*, 70(4):447–457, 1997. ISSN 0044-0086.

Geoff J. M. Parker, Caleb Roberts, Andrew Macdonald, Giovanni A. Buonaccorsi, Sue Cheung, David L. Buckley, Alan Jackson, Yvonne Watson, Karen Davies, and Gordon C. Jayson. Experimentally-derived functional form for a population-averaged high-temporal-resolution arterial input function for dynamic contrast-enhanced MRI. *Magnetic Resonance in Medicine*, 56(5):993–1000, November 2006. ISSN 0740-3194. doi: 10.1002/mrm.21066.

Raymond Queneau. *Zazie dans le métro*. Gallimard, 1959.

Eduard Rohan, Jana Turjanicová, and Vladimír Lukeš. Multiscale modelling and simulations of tissue perfusion using the Biot-Darcy-Brinkman model. *Computers & Structures*, 251:106404, July 2021a. ISSN 0045-7949. doi: 10.1016/j.compstruc.2020.106404.

Eduard Rohan, Jana Camprová Turjanicová, and Václav Liška. Geometrical model of lobular structure and its importance for the liver perfusion analysis. *PLOS ONE*, 16(12):e0260068, December 2021b. ISSN 1932-6203. doi: 10.1371/journal.pone.0260068.

Ryan J. Schulze, Micah B. Schott, Carol A. Casey, Pamela L. Tuma, and Mark A. McNiven. The cell biology of the hepatocyte: A membrane trafficking machine. *Journal of Cell Biology*, 218(7):2096–2112, June 2019. ISSN 0021-9525. doi: 10.1083/jcb.201903090.

Timothy W. Secomb and Axel R. Pries. Blood viscosity in microvessels: Experiment and theory. *Comptes Rendus Physique*, 14(6):470–478, June 2013. ISSN 16310705. doi: 10.1016/j.crhy.2013.04.002.

Masanori Tachikawa, Yuna Sumiyoshiya, Daisuke Saigusa, Kazunari Sasaki, Michitoshi Watanabe, Yasuo Uchida, and Tetsuya Terasaki. Liver Zonation Index of Drug Transporter and Metabolizing Enzyme Protein Expressions in Mouse Liver Acinus. *Drug Metabolism and Disposition*, 46(5):610–618, May 2018. ISSN 0090-9556, 1521-009X. doi: 10.1124/dmd.117.079244.

Harald F. Teutsch. The modular microarchitecture of human liver. *Hepatology*, 42(2):317–325, August 2005. ISSN 0270-9139, 1527-3350. doi: 10.1002/hep.20764.

Evita van de Steeg, Viktor Stránecký, Hana Hartmannová, Lenka Nosková, Martin Hřebíček, Els Wagenaar, Anita van Esch, Dirk R. de Waart, Ronald P. J. Oude Elferink, Kathryn E. Kenworthy, Eva Sticová, Mohammad al-Edreesi, A. S. Knisely, Stanislav Kmoch, Milan Jirsa, and Alfred H. Schinkel. Complete OATP1B1 and OATP1B3 deficiency causes human Rotor syndrome by interrupting conjugated bilirubin reuptake into the liver. *The Journal of Clinical Investigation*, 122(2):519–528, February 2012. ISSN 1558-8238. doi: 10.1172/JCI59526.

Nachiket Vartak, Dirk Drasdo, Fabian Geisler, Tohru Itoh, Ronald P.J.Oude Elferink, Stan F.J. Graaf, John Chiang, Verena Keitel, Michael Trauner, Peter Jansen, and Jan G. Hengstler. On the Mechanisms of Biliary Flux. *Hepatology*, 74(6):3497–3512, December 2021a. ISSN 0270-9139, 1527-3350. doi: 10.1002/hep.32027.

Nachiket Vartak, Georgia Guenther, Florian Joly, Amruta Damle-Vartak, Gudrun Wibbelt, Jörns Fickel, Simone Jörs, Brigitte Begher-Tibbe, Adrian Friebel, Kasimir Wansing, Ahmed Ghallab, Marie Rosselin, Noemie Boissier, Irene Vignon-Clementel, Christian Hedberg, Fabian Geisler, Heribert Hofer, Peter Jansen, Stefan Hoehme, Dirk Drasdo, and Jan G. Hengstler. Intravital Dynamic and Correlative Imaging of Mouse Livers Reveals Diffusion-Dominated Canalicular and Flow-Augmented Ductular Bile Flux. *Hepatology*, 73(4):1531–1550, April 2021b. ISSN 0270-9139, 1527-3350. doi: 10.1002/hep.31422.

Appendices

Appendix A

Analytical Resolution of the Equations for Double Perfusion

For the sake of completeness as well as for future reference, we solve the 1D equations for double perfusion, modelling for example the flows in blood and bile. The equations themselves are adapted from Rohan et al. [2021b]. We will describe the solution process in detail here, complementing it by several illustrative plots.

We start by assuming that flow in both blood and bile compartments is stationary and can be described as porous medium flow using *Darcy's law*. If we denote the permeabilities in blood and bile as $H^{(S)}$ and $H^{(B)}$ respectively, the pressures as $p^{(S)}$ and $p^{(B)}$ respectively, and finally the permeability of the two compartments as G, then the equations for flow read

$$
\begin{cases}
-\dfrac{\partial}{\partial z}\left(H^{(S)}\dfrac{\partial p^{(S)}}{\partial z}\right) + G\left(p^{(S)} - p^{(B)}\right) = 0, \\[2ex]
-\dfrac{\partial}{\partial z}\left(H^{(B)}\dfrac{\partial p^{(B)}}{\partial z}\right) + G\left(p^{(B)} - p^{(S)}\right) = 0,
\end{cases}
\tag{A.1}
$$

assuming no external forces are exerted on the system.

To solve this system (A.1) analytically, we start by rewriting it in vectorial form as

$$
-\frac{\partial}{\partial z}\left(\mathbb{H}\frac{\partial \boldsymbol{p}}{\partial z}\right) + \mathbb{G}\boldsymbol{p} = \boldsymbol{0},
\tag{A.2}
$$

where we have defined

$$
\mathbb{H} := \begin{bmatrix} H^{(S)} & 0 \\ 0 & H^{(B)} \end{bmatrix}, \quad
\mathbb{G} := G \begin{bmatrix} 1 & -1 \\ -1 & 1 \end{bmatrix}, \quad
\boldsymbol{p} := \begin{bmatrix} p^{(S)} \\ p^{(B)} \end{bmatrix}.
$$

Next, we introduce the substitution

$$
\boldsymbol{q} := \mathbb{H}^{\frac{1}{2}}\boldsymbol{p}, \quad \mathbb{W} := \mathbb{H}^{-\frac{1}{2}}\mathbb{G}\mathbb{H}^{-\frac{1}{2}},
$$

under which Equation (A.2) transforms to

$$
-\frac{\partial^2 \boldsymbol{q}}{\partial z^2} + \mathbb{W}\boldsymbol{q} = \boldsymbol{0}.
$$

Solving the above equation analytically is reasonably straightforward. We start by transforming it into the eigenbasis of $\mathbb{W}$, proceeding then to solve the two

resulting scalar linear ODEs. The final result, in original variables, reads

$$\boldsymbol{p} = \mathbb{H}^{-\frac{1}{2}} \left[(az + b)\boldsymbol{r}_1 + \left(c e^{\sqrt{\lambda_2} z} + d e^{-\sqrt{\lambda_1} z} \right) \boldsymbol{r}_2 \right],$$

where λ_i, $\boldsymbol{r}_i$ are eigenvalues and eigenvectors of $\mathbb{W}$ respectively. The integration constants $a, b, c, d \in \mathbb{R}$ must be determined from the boundary conditions. It can be readily shown that

$$\lambda_1 = 0, \quad \lambda_2 = G \left(\frac{1}{H^{(S)}} + \frac{1}{H^{(B)}} \right) > 0,$$

and one of the possible choices of eigenvectors is

$$\boldsymbol{r}_1 = \begin{bmatrix} \sqrt{H^{(S)}} \\ \sqrt{H^{(B)}} \end{bmatrix}, \quad \boldsymbol{r}_2 = \begin{bmatrix} -\sqrt{\frac{1}{H^{(S)}}} \\ \sqrt{\frac{1}{H^{(B)}}} \end{bmatrix}.$$

The velocity fields are then given by Darcy's law as

$$v_z^{(S,B)} = -H^{(S,B)} \frac{\partial p^{(S,B)}}{\partial z}.$$

There are multiple ways of prescribing boundary conditions to this system. Several possibilities are illustrated in Figure A.1. The exact boundary conditions were

- $p^{(S)}\big|_{z=0} = 0.01,\ v_z^{(S)}\big|_{z=L} = 0,\ v_z^{(B)}\big|_{z=0} = 0,\ p^{(S)}\big|_{z=0} = 0.02$ in Figure A.1a,

- $p^{(S)}\big|_{z=0} = 2,\ p^{(S)}\big|_{z=L} = 3,\ v_z^{(B)}\big|_{z=0} = v_z^{(B)}\big|_{z=L} = 0$ in Figure A.1b,

- $v_z^{(S)}\big|_{z=0} = v_z^{(B)}\big|_{z=0} = 0,\ p^{(S)}\big|_{z=L} = 3,\ p^{(B)}\big|_{z=L} = 2$ in Figure A.1c.
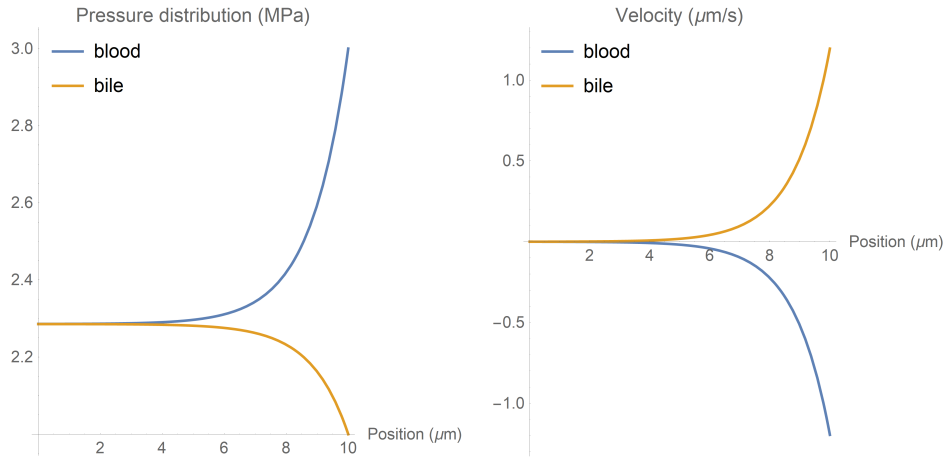
In all above plots, we set model parameters to $L = 10$, $H^{(S)} = 2$, $H^{(B)} = 5$, $G = 1$.
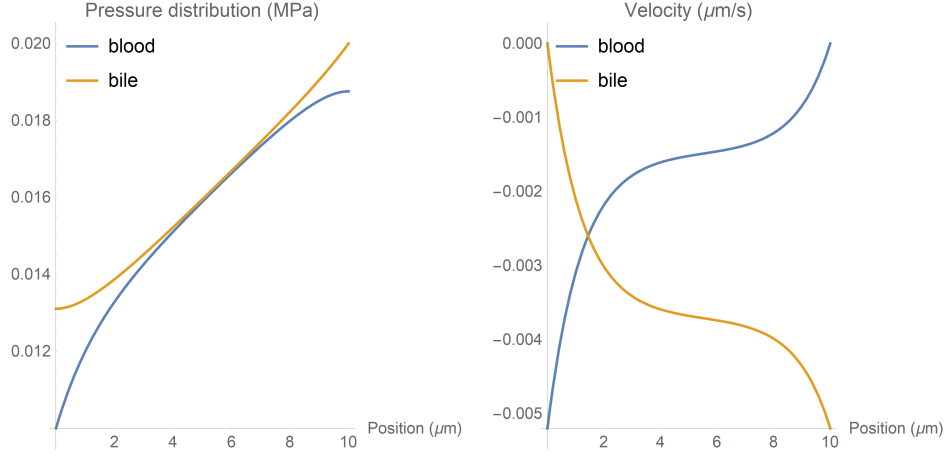
(a) $p^{(\mathrm{S})}\big|_{z=0} = 0.01$, $v_z^{(\mathrm{S})}\big|_{z=L} = 0$, $v_z^{(\mathrm{B})}\big|_{z=0} = 0$, $p^{(\mathrm{S})}\big|_{z=0} = 0.02$
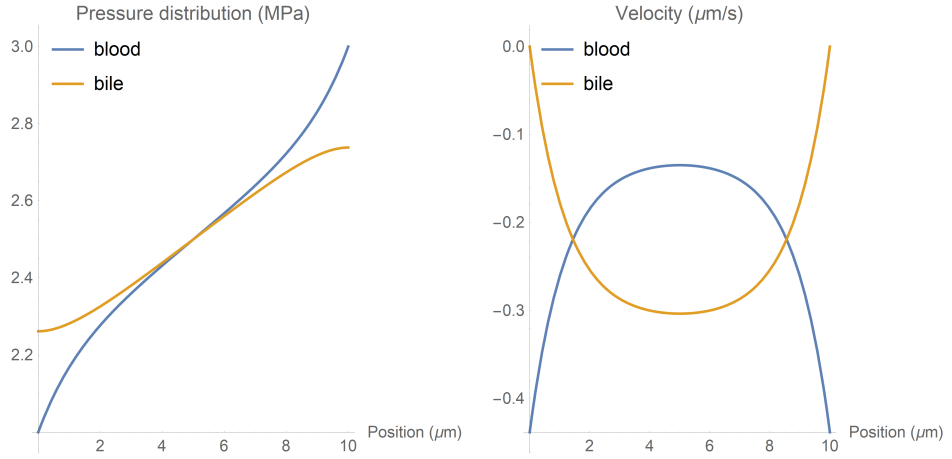
(b) $p^{(\mathrm{S})}\big|_{z=0} = 2$, $p^{(\mathrm{S})}\big|_{z=L} = 3$, $v_z^{(\mathrm{B})}\big|_{z=0} = v_z^{(\mathrm{B})}\big|_{z=L} = 0$

(c) $v_z^{(\mathrm{S})}\big|_{z=0} = v_z^{(\mathrm{B})}\big|_{z=0} = 0$, $p^{(\mathrm{S})}\big|_{z=L} = 3$, $p^{(\mathrm{B})}\big|_{z=L} = 2$

Figure A.1: In the plots above, we see pressure distributions and velocities in the blood and bile compartments given by the double perfusion model from Equation (A.1) for different boundary conditions. The parameters used in these examples were $L = 10$, $H^{(\mathrm{S})} = 2$, $H^{(\mathrm{B})} = 5$, $G = 1$, and the boundary conditions are specified below each plot.

Appendix B

Test Cases for Advection-Diffusion-Reaction Solvers

As the numerical implementation of the compartment model contains solver algorithms explicitly instead of relying on calls to third-party solver libraries, it is crucial to have a series of tests verifying that the algorithms are indeed implemented correctly. These tests take the form of special problem settings with analytic solutions, so that we can compare the computed result with the expected analytical expression.

Since the implementation of the ODE solver is relatively straightforward, in the following sections we concentrate rather on the finite volume solver used in the Blood and Bile compartments. We look for analytic solutions of the advection-diffusion-reaction equation

$$\frac{\partial c}{\partial t} + v\frac{\partial c}{\partial x} - D\frac{\partial^2 c}{\partial x^2} = f \tag{B.1}$$

under several simplifying assumptions that lead to different analytically solvable scenarios, together verifying the correctness of implementation of all key components of the model.

For the sake of simplicity, we solve all initial-boundary-value problems (IBVPs) below on $(t, x) \in \mathbb{R}^+ \times (0, 1)$.

B.1 Advection-Reaction

We start with the case $D = 0$, where Equation (B.1) reduces to an *advection-reaction* equation. At the inlet, the boundary condition is given by an input function $g(t)$, following the setting of the actual model. When prescribing explicit forms of the right-hand side f, motivated by the two asymptotic regimes of Michaelis-Menten kinetics, we consider

1. a *constant* right-hand side $f(c(t, x), t, x) := f_1 \in \mathbb{R}$,

2. a *linear* right-hand side $f(c(t, x), t, x) := f_1 c(t, x)$, $f_1 \in \mathbb{R}$.

The initial condition is set to allow for a simple analytic solution, so that the IBVP reads

$$\frac{\partial c}{\partial t} + v \frac{\partial c}{\partial x} = f_1 \quad \text{in } \mathbb{R}^+ \times (0,1), \quad c|_{t=0} = g\left(-\frac{x}{v}\right) + f_1 \frac{x}{v}, \quad c|_{x=0} = g(t)$$

for the constant right-hand side, and

$$\frac{\partial c}{\partial t} + v \frac{\partial c}{\partial x} = f_1 c \quad \text{in } \mathbb{R}^+ \times (0,1), \quad c|_{t=0} = g\left(-\frac{x}{v}\right) e^{f_1 \frac{x}{v}}, \quad c|_{x=0} = g(t)$$

for the linear right-hand side. The corresponding analytic solutions (adapted from the work of Boissier et al. [2021]) are

$$c(t,x) = g\left(t - \frac{x}{v}\right) + f_1 \frac{x}{v}, \quad c(t,x) = g\left(t - \frac{x}{v}\right) e^{f_1 \frac{x}{v}},$$

respectively.

The results of the two test cases for the advection-reaction scenario are shown in Figures B.1 and B.2. Parameters used in these test simulations were

- time step: 0.001,

- space step: 0.01,

- $v = 1$,

- $f_1 = 1$ (corresponding to $f = f_1$ and $f = f_1 c$ in the two scenarios),

- $g(t) = e^{-10(t-3)^2}$.

We can see that the numerical solution reproduces the analytical expression considerably well in both cases. However, the correspondence is not perfect, and the two differ mostly in regions where the solutions undergo faster variations. This is a minor issue that can be overcome by either refining the spatial and temporal discretizations, or by using a higher order numerical scheme, as presented by Boissier et al. [2021].

B.2 Steady-State Limit of Advection-Diffusion

In the model presented in this thesis, we add a diffusion term on top of the transport equations solved, e.g., by Boissier et al. [2021], which means that the above tests do not serve as complete validation of the solver implementation. To test the diffusion element in the simulation code, rather than comparing against a fully analytic solution, we study the asymptotic behavior of a solution to the homogeneous advection-diffusion equation whose steady state is expected to be constant. That is, we solve numerically the IBVP

$$\frac{\partial c}{\partial t} + v \frac{\partial c}{\partial x} - D \frac{\partial^2 c}{\partial x^2} = 0 \quad \text{in } \mathbb{R}^+ \times (0,1),$$

$$c|_{t=0} = \frac{5}{2} - 3\left|x - \frac{1}{2}\right|, \quad c|_{x=0} = 0, \quad D\nabla c \cdot \boldsymbol{n}|_{x=1} = 0,$$

expecting that, asymptotically, the solution would tend to 1 on the whole interval $(0,1)$. The initial condition is chosen for illustrative purposes, as it allows to observe the main properties of the numerical scheme used (cf. discussion of results below). The boundary conditions are chosen in analogy with the choice made in the actual compartment model, and we refer to Sections 3.1 and 4.1.3 for a more detailed discussion.

For the sake of completeness, three test simulations were performed – one for pure advection, one for pure diffusion, and one for advection-diffusion. The simulation parameters were set to

- time step: 5×10^{-4},

- space step: 0.01,

- $v = 1$ ($v = 0$ for pure diffusion),

- $D = 1$ ($D = 0$ for pure advection),

and the results of the tests are shown in Figures B.3, B.4, and B.5.

The numerical solutions in all three test cases reproduce the expected behavior, at least qualitatively. One notable feature, best seen in Figure B.3, is the numerical diffusion that is inherent to the used scheme, and results in smoothing of the contour of the initial condition. This effect would be even more prominent for a scheme of higher order in space, and it is very undesirable in view of the intended practical application (cf. Boissier et al. [2021]). To overcome numerical diffusion, *slope limiters* can be introduced into the numerical schemes to counteract the diffusive properties of higher-order schemes (cf. discussion by Boissier et al. [2021] and more extensively LeVeque [2002]).
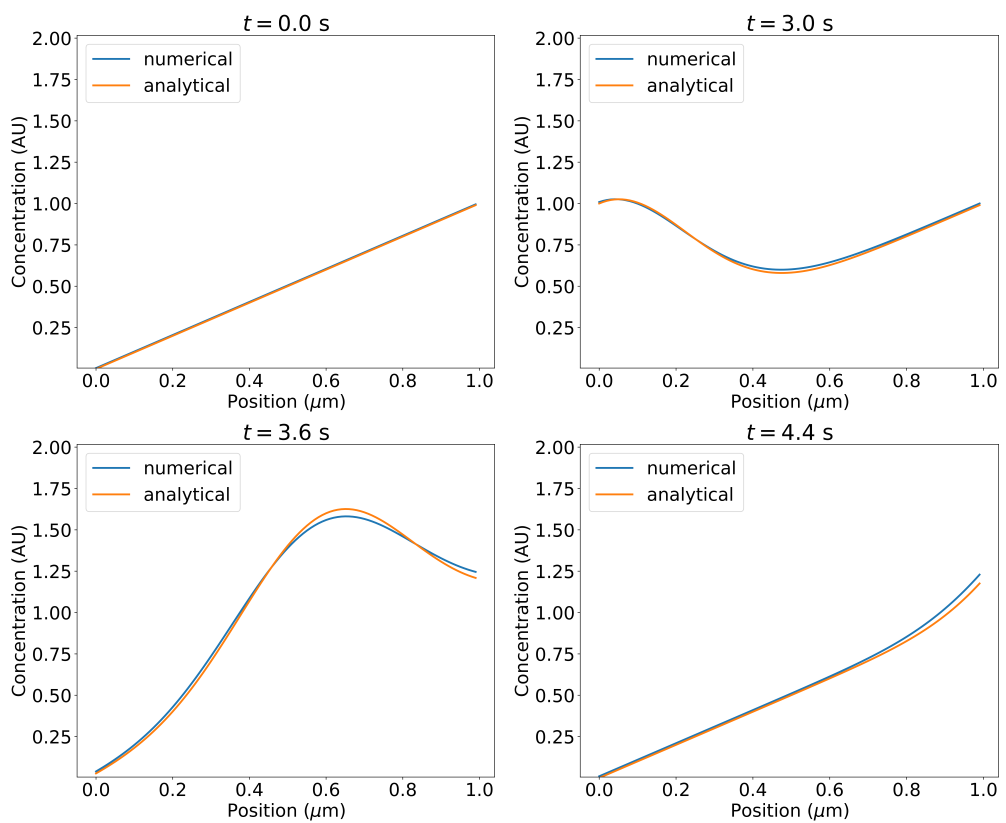
Figure B.1: Results of the test for the advection-reaction scenario with constant right-hand side. As we can see, the numerical and the analytical solutions are reasonably close for this precision, although there are slight differences, especially in region where the solutions vary considerably. This is only a minor issue that can be overcome by using finer discretizations in time and space or a higher order numerical scheme.
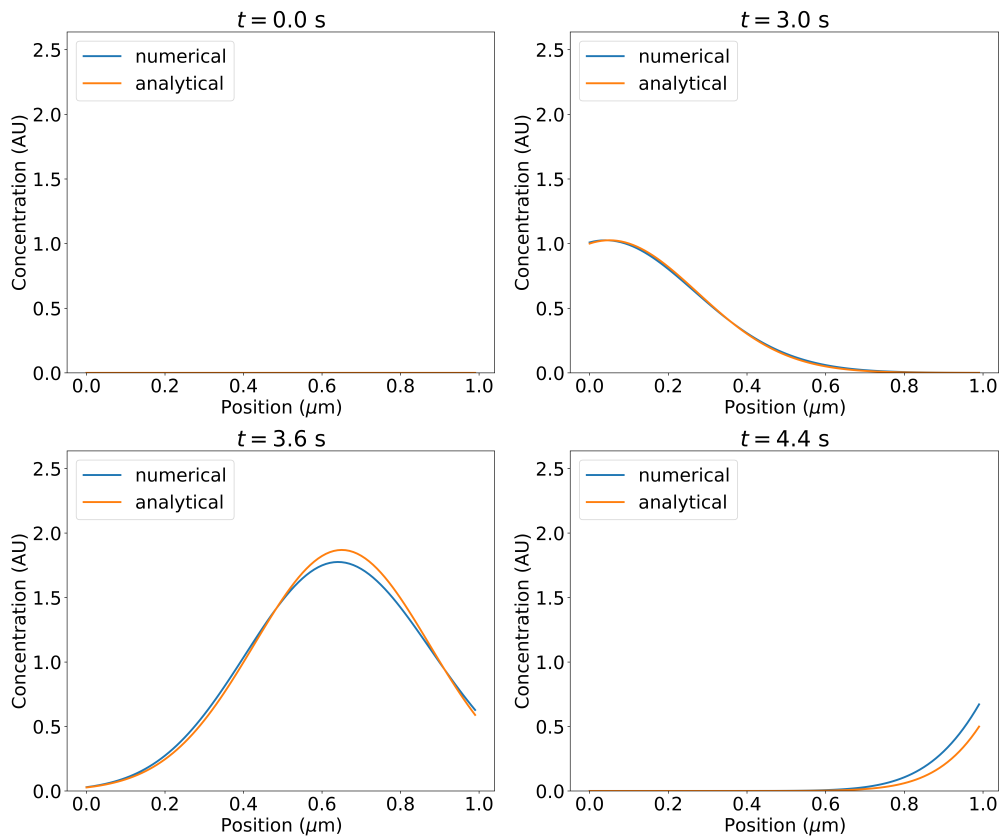
Figure B.2: Results of the test for the advection-reaction scenario with linear right-hand side. Again, the numerical and the analytical solutions are close except for regions with faster variation in the solutions. As for the constant case, a finer discretization or a higher order numerical scheme would help overcome this issue.
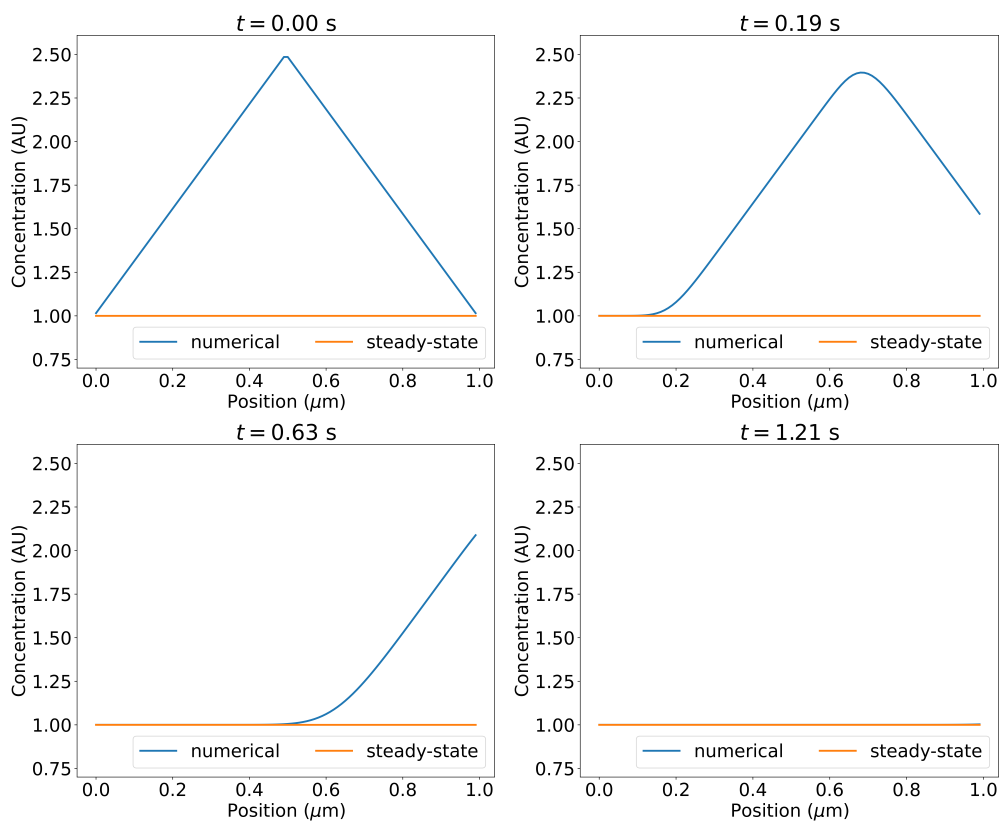
Figure B.3: Steady-state behavior of the numerical solution in a pure advection scenario. We can see that the overall behavior of the solution is as expected – the initial condition is merely transported out of the computational domain. We do see however non-negligible smoothing of the solution due to numerical diffusion. This is an unwanted effect that can be suppressed by adding slope limiters into the numerical schemes.
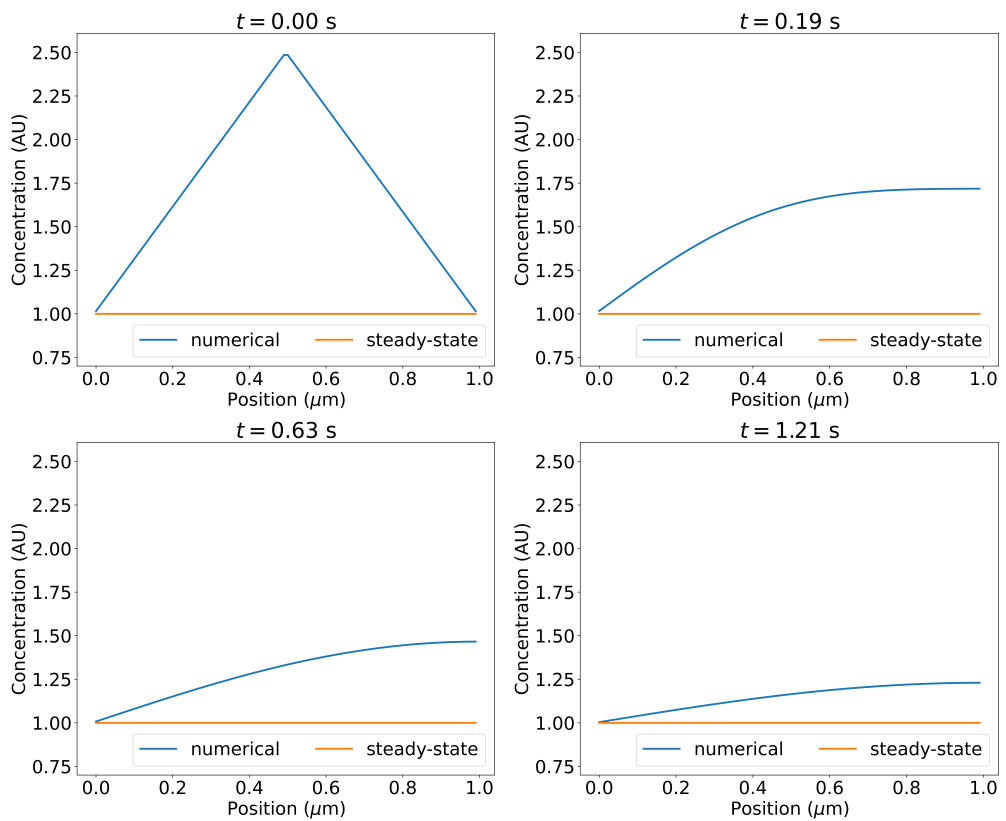
Figure B.4: Steady-state behavior of the numerical solution in a pure diffusion scenario. The results agree with the expected behavior of a solution to the diffusion equation. The asymmetry in the solution at $t > 0$ is given by the difference in boundary conditions imposed at $x = 0$ and $x = 1$.
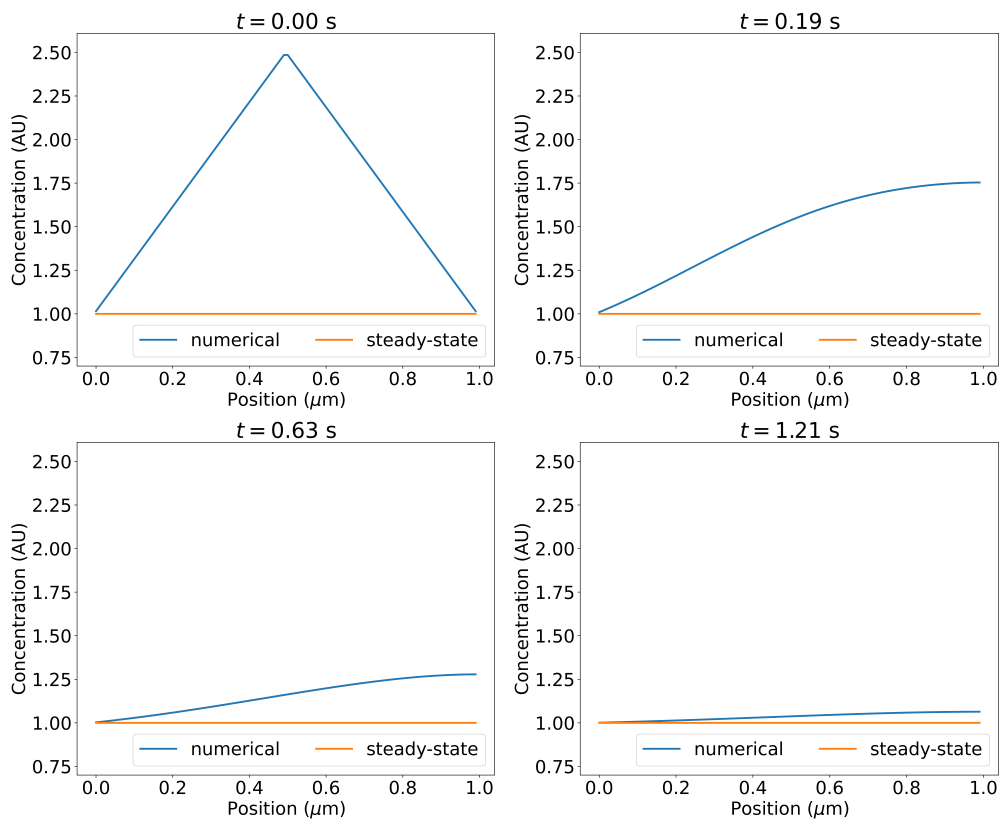
Figure B.5: Steady-state behavior of the numerical solution in an advection-diffusion scenario. We see that the solution is very similar to the pure diffusion test case, but we can see that the diffusive behavior is enhanced by advective transport, resulting in the initial condition "disappearing faster" from the computational domain.

Appendix C

Source Code Repository

The source code for the simulations presented in Chapter 3 is openly available on a GitLab repository at Inria. The code is bound to be modified even after the submission of the thesis, but the state of the repository relevant to the thesis is stored under the tag `v1.0-thesis-submission` on the following link: `https://gitlab.inria.fr/pkottman/bile-compartment-model/-/tree/v1.0-thesis-submission`.